

Research Paper

# Engineering of donor-acceptor-donor curcumin analogues as near-infrared fluorescent probes for *in vivo* imaging of amyloid- $\beta$ species

Daqing Fang<sup>1,3#</sup>, Xidan Wen<sup>2#</sup>, Yuqi Wang<sup>2</sup>, Yidan Sun<sup>2</sup>, Ruibing An<sup>2</sup>, Yu Zhou<sup>3</sup>, Deju Ye<sup>2✉</sup>, Hong Liu<sup>1,3✉</sup>

1. Key Laboratory of Structure-Based Drug Design and Discovery, Ministry of Education, Shenyang Pharmaceutical University, Shenyang, 110016, China.
2. State Key Laboratory of Analytical Chemistry for Life Sciences, Chemistry and Biomedicine Innovation Center (ChemBIC), School of Chemistry and Chemical Engineering, Nanjing University, Nanjing, 210023, China.
3. State Key Laboratory of Drug Research, Shanghai Institute of Materia Medica, Chinese Academy of Sciences, Shanghai, 201203, China.

#These authors have contributed equally to this work.

✉ Corresponding authors: Hong Liu, E-mail: hliu@simm.ac.cn; Deju Ye, E-mail: dejuye@nju.edu.cn.

© The author(s). This is an open access article distributed under the terms of the Creative Commons Attribution License (<https://creativecommons.org/licenses/by/4.0/>). See <http://ivyspring.com/terms> for full terms and conditions.

Received: 2021.11.03; Accepted: 2022.02.28; Published: 2022.04.04

## Abstract

Near-infrared (NIR) fluorescent imaging of both soluble and insoluble A $\beta$  species in the brain of Alzheimer's disease (AD) is crucial for the early diagnosis and intervention of AD. To date, a variety of NIR fluorescent probes have been reported for the detection of A $\beta$  species. Among these probes, CRANAD-58 was reported to have the capability to detect both soluble and insoluble A $\beta$  species, which is vital to monitor the changes of A $\beta$  species during the pathological course of the disease. Though CRANAD-58 has shown promise to noninvasively detect A $\beta$  species in transgenic AD mice, the emission wavelength (~670 nm) is still too short for further applications. Therefore, new probes with longer emission wavelength and improved physiological properties are in highly demand. Herein, we report the design and engineering of nine donor-acceptor-donor molecules as "off-on" near-infrared fluorescent probes for *in vivo* imaging of both soluble and insoluble A $\beta$  species in living AD mice owing to its improved *in vitro* properties and *in vivo* performance.

**Methods:** We report a two-round strategy to develop nine "off-on" NIR fluorescence probes via structural modification of a curcumin analogue-based donor-acceptor-donor architecture. In round one, probes **1** and **2** were synthesized, and probe **2** was identified to be an optimum probe as it showed distinct "off-on" NIR fluorescence at > 690 nm upon binding to A $\beta$  monomers, oligomers and aggregates. To further improve the *in vivo* performance, further structural modification of probe **2** into probes **3-9** was then conducted. The fluorescence response with A $\beta$  species and histological staining *in vitro* and *in vivo* imaging of A $\beta$  species in APP/PS1 transgenic AD mice and age-matched wild-type mice were performed.

**Results:** We demonstrate that, compared to probe **2**, probe **9** with improved physiological properties hold the fastest kinetics (~10 min) to produce not only higher brain fluorescence intensity in 10-month-old APP/PS1 transgenic AD mice, but also afford a higher discrepancy in brain fluorescence to discriminate AD mice from wild-type (WT) mice. Probe **9** also hold the ability to detect soluble A $\beta$  species in 6-month-old APP/PS1 transgenic mice. Probe **9** was further applied for dynamic visualization of A $\beta$  plaques in a skull-thinning 14-month-old APP/PS1 mouse, which revealed its immediate penetration into brain parenchyma and selective labeling of both parenchymal and angiopathic A $\beta$  plaques. In addition, probe **9** possessed significantly high attenuation effect on the aggregation of A $\beta$  monomers.

**Conclusion:** Our results demonstrate the good potential of probe **9** for longitudinal NIR fluorescence imaging of soluble and insoluble A $\beta$  species in APP/PS1 transgenic AD mice, which may act as a useful tool for early diagnosis and intervention of AD.

Key words: Alzheimer's disease; Amyloid- $\beta$ ; NIR fluorescence probe; *in vivo* imaging; D-A-D molecules

## Introduction

Alzheimer's disease (AD) is one of the most notorious neurodegenerative diseases, which progressively causes cognitive decline, irreversible memory loss, and disorientation. AD occurs with several pathological hallmarks, such as aggregation of amyloid- $\beta$  ( $A\beta$ ) peptides into fibrils and plaques, formation of tau protein tangles, and upregulation of reactive oxygen species (ROS) [1-3]. It has been recognized that  $A\beta$  species, including soluble monomers, dimers, oligomers, and insoluble fibrils/aggregates and plaques, can exert high toxicity against neuronal cells [4, 5]. During the course of AD progression, all types of  $A\beta$  species are present, with the predominance of the subspecies progressively changing from soluble species to insoluble fibrils and plaques [6]. Methods capable of detecting both soluble and insoluble  $A\beta$  species can provide the potential to monitor the progression of AD, which are desirable for early definitive diagnosis of AD.

Over the past decades, tremendous efforts have been devoted to detect  $A\beta$  species, and molecular imaging techniques, such as magnetic resonance imaging (MRI) [7], single-photon emission-computed tomography (SPECT) [8], positron emission computed tomography (PET) [9], and optical imaging [10] have shown promise due to the advantages of non-invasiveness, and real-time manner, allowing to monitor the progression of AD at molecular and cellular levels. Till now, a few PET tracers, such as  $^{18}\text{F}$ -labeled florbetapir, flutemetamol and florbetaben, have been approved for the detection of  $A\beta$  plaques in clinics [11-14], while the use of radioactive isotopes requires expensive cyclotron and well skilled chemists, which will place high cost to the patients; additionally, the unavoidable exposure to radiation from administrated radiotracers has also impeded their routine applications. Alternately, people have developed a number of fluorescent probes, such as Congo Red (CR), Thioflavin T (ThT) and Pittsburgh B (PIB), for the detection of  $A\beta$  species as fluorescence imaging possesses much lower cost, easier operation and avoidance of radiation exposure compared to PET imaging [15]. Particularly, many fluorescent probes with their emission in the near infrared (NIR) region ( $\lambda > 650$  nm) capable of improving tissue penetration depth and reducing autofluorescence of biological tissues, have emerged as promising tools for *in vivo* imaging of  $A\beta$  deposits and helping diagnosis of AD [16-34]. Most NIR fluorescent probes for  $A\beta$  species have been designed to have an electron donor (D)-acceptor (A) or D-A-D architecture, which showed weak NIR fluorescence in aqueous solution, but strong fluorescence upon binding to  $A\beta$  species [10]. For example, Swager reported NIAD-4 with a

D-A architecture as the first NIR fluorescent probe for *in vivo* imaging of  $A\beta$  plaques [35], however, the relatively short absorption and emission wavelength ( $\lambda_{\text{ex/em}} = 475/612$  nm) could allow it to work only in cranial window-implanted transgenic AD mice under two-photon excitation. Saji and coworkers lately employed a boron dipyrromethane (BODIPY) fluorophore as the acceptor and a dimethylamino styryl group as the donor, and reported a new D-A type of NIR fluorescent probe (BAP-1) [36], which showed longer absorption and emission wavelengths ( $\lambda_{\text{ex/em}} = 604/648$  nm) than that of NIAD-4 [35]; however, the nonspecific distribution in the scalp largely lowered the *in vivo* imaging ability. Cui and coworkers reported another series of D-A molecules (DANIRs) by linking the electron-donating *N,N'*-dimethylamino group (D) and electron-accepting malononitrile group (A) through varying lengths of  $\pi$ -conjugated bonds [22-27, 32, 37]; probe (3c) [24] showed a remarkably enhanced NIR fluorescence ( $\lambda_{\text{em}} = 678$  nm) upon binding with  $A\beta$  aggregates and could efficiently penetrate the blood brain barrier (BBB) to differentiate transgenic AD mice from wild-type mice through noninvasive fluorescence imaging. Ran *et al.* [17-21, 38] reported curcumin analogues with a D-A-D architecture as prominent NIR fluorescent probes, and among them, CRANAD-58 displayed high affinities not only to the insoluble  $A\beta$  aggregates, but also to soluble  $A\beta$  monomers and oligomers, offering enhanced NIR fluorescence emission ( $\lambda_{\text{ex/em}} \approx 580/670$  nm) to noninvasively detect  $A\beta$  species in transgenic AD mice [18]. Despite encouraging progresses made, there is still challenging to design high performance NIR fluorescence probes capable of fast crossing BBB and noninvasively detecting  $A\beta$  species, particularly soluble  $A\beta$  monomers and oligomers with high sensitivity and specificity. Such probes could be amenable for the detection of AD at an early stage, grateful for early intervention of AD prior to the appearance of obvious symptoms.

Herein, we report a two-round strategy to develop sensitive "off-on" NIR fluorescence probes by modifying CRANAD-58 with a D-A-D chemical architecture. In round one, we designed probes **1** and **2**, and identified probe **2** was an optimum probe, which showed improved fluorescence quantum yield ( $\Phi_f$ ) and red-shifted absorption and fluorescence emission over CRANAD-58 upon binding to either insoluble  $A\beta$  aggregates or soluble  $A\beta$  monomers and oligomers. Based on probe **2**, the second round of modification allowed us to design probes **3-9** by improving binding affinity, augmenting fluorescence turn-on ratio and balancing lipophilicity to improve brain uptake. Following systemic administration, we

demonstrated that probes **2**, **4**, **6** and **9** with good *in vitro* performance could rapidly cross BBB and produce significantly brighter NIR fluorescence in the brains of APP/PS1 transgenic AD mice compared to the age-matched WT mice. We further employed an upright microscope to dynamically visualize the entry of probe **9** into brain parenchyma and selective labeling of both parenchymal and angiopathic A $\beta$  plaques in a skull-thinning 14-month-old APP/PS1 mouse, not in WT mice. Additionally, as shown in Figure 1A, the mechanism of designed probes for fluorescence imaging of A $\beta$  species in living mice of AD model was proposed. Following intravenous administration, the probes can cross the BBB and enter into brain. In the absence of A $\beta$  species, these probes with the D-A-D architecture possess a substantial degree of conformational freedom and a non-radiative decay process dominates, thus exhibiting weak fluorescence. However, in the brain with A $\beta$  species existence, the probes can bind to the A $\beta$  species and the conformation is restricted, which substantially decreases the vibrational-rotational processes, leading to an increase in the radiative decay rate. Thus, enhanced NIR fluorescence appeared, which can provide sensitive signals to noninvasively visualize the A $\beta$  species in the brains of living AD mice.

## Materials and Methods

### Materials

All chemical reagents were reagent grade and used as purchased from commercial sources (such as Aldrich, Adamas) without further purification. A $\beta$  (1-42) monomer was purchased from Nanjing Peptide Biotech Ltd. (Nanjing, China). High glucose Dulbecco's Modified Eagle's Medium (DMEM), fetal bovine serum (FBS), penicillin/streptomycin were purchased from Thermo (Shanghai, China). 3-(4,5-Dimethylthiazol-2-yl)-2,5-diphenyltetrazolium bromide (MTT) kit was obtained from KeyGen Biotech. Co. Ltd. (Nanjing, China). Normal ICR mice (5 weeks, male), BALB/c mice (5 weeks, female), Transgenic mice (C57BL6, APP<sup>swe</sup>/PSEN1, 4-14 months old, male), and its littermates were purchased from the Model Animal Research Center (MARC) of Nanjing University (Nanjing, China). All animal experiments were approved by the Institutional Animal Care and Use Committee (IACUC) of Nanjing University.

### Preparation of A $\beta$ 42 monomers, oligomers and aggregates

A $\beta$  monomers were prepared by dissolving commercial A $\beta$ <sub>42</sub> peptide in hexafluoroisopropanol at

a concentration of 250  $\mu$ M as a stock.

A $\beta$ <sub>42</sub> oligomers was prepared according to the procedure reported previously [39], and confirmed by TEM. Briefly, Soluble oligomers were prepared by dissolving 1.0 mg A $\beta$  in 400  $\mu$ L hexafluoroisopropanol (HFIP) at room temperature and stayed for 15 min. 100  $\mu$ L of the resulting A $\beta$  solution was added to 900  $\mu$ L D.I. H<sub>2</sub>O in a siliconized Eppendorf tube. After incubation at room temperature for another 15 min, the samples were centrifuged at 14,000  $\times$  G for 15 min, and the supernatant was transferred to a new siliconized tube and subjected to a gentle stream of N<sub>2</sub> for 10 min to evaporate the HFIP. The samples were then stirred at 500 rpm using a Teflon coated micro stir bar at  $\sim$ 22  $^{\circ}$ C for 24-48 h.

To prepare A $\beta$ <sub>42</sub> aggregates, the A $\beta$ <sub>42</sub> peptide (1.0 mg) was suspended in 1% ammonia hydroxyl solution (1.0 mL). One hundred microliters of the resulting solution were diluted 10-fold with PBS buffer (pH = 7.4), and kept stirring at room temperature for 3 days. TEM analysis was applied to confirm the formation of A $\beta$  aggregates.

### Response of probes toward A $\beta$ species

To test interaction of each probe with A $\beta$  species, the following procedure was utilized. (1) Each probe was added to 2.0 mL PBS buffer (pH = 7.4) (250 nM of final concentration); (2) A $\beta$  species (25  $\mu$ M stock solution in HFIP for monomers, and 25  $\mu$ M stock solution in PBS buffer or D.I. water for oligomers and aggregates) were added to the probe solution to make the final A $\beta$  species concentration of 250 nM; (3) the mixture was transferred to quartz cuvette and its fluorescence spectra were recorded by HORIBA Jobin Yvon Fluoromax-4 fluorometer; (4) the fluorescence spectra of PBS buffer or each probe in PBS buffer alone was also measured using the same parameters in (3). The fold increase of the fluorescence intensity after binding to the A $\beta$  species was calculated by the following equation:

$$\text{Fold enhancement} = (FI_{\text{test}} - FI_{\text{PBS}}) / (FI_{\text{probe}} - FI_{\text{PBS}})$$

Where  $FI_{\text{test}}$ ,  $FI_{\text{probe}}$  and  $FI_{\text{PBS}}$  represent the fluorescence intensities of probes upon binding to A $\beta$  species, the solution of probes in PBS, and PBS alone, respectively.

### TEM Measurement

Ten microliters of 250 nM of A $\beta$ <sub>42</sub> oligomers or aggregates in PBS solution were pipetted onto a carbon-coated copper grid, followed by the addition of 10  $\mu$ L of a PTA staining solution to the grid. After 1 min, the liquid on the grid was carefully dried with a corner of filter paper, and the resulting grid was further dried in the air for 10 min. The TEM images were obtained with the JEM-1011 TEM.

## Confocal fluorescence imaging of A $\beta$ oligomers or A $\beta$ aggregates

To a PBS buffer (pH = 7.4) solution of A $\beta$  oligomers or A $\beta$  aggregates (25  $\mu$ M), probe **2** was added to be a final concentration of 2.5  $\mu$ M. After being mixed, the solution of A $\beta$  oligomers or A $\beta$  aggregates was added to a glass slide and covered with a cover glass respectively. Fluorescence images were captured on a Leica TCS SP8 confocal laser scanning microscope, with the excitation wavelength at 620 nm, and the emission wavelength from 650 nm to 750 nm.

## <sup>1</sup>H-NMR studies with KLVFF segment

<sup>1</sup>H-NMR spectrum of DMSO-*d*<sub>6</sub> solution of KLVFF (2.0 mM) was recorded at 25 °C using 500 MHz Bruker Avance III HD 500 spectrometer followed by addition of probe **2** (2.0 mM) and probe **9** (2.0 mM). The resulting solution was kept at room temperature overnight, and then subjected to <sup>1</sup>H-NMR spectrum acquirement. The ppm reference peaks were set at 2.49 ppm with DMSO-*d*<sub>6</sub> as the reference.

## Binding constant (K<sub>d</sub>) measurement

The concentration of each probe was determined by weight method. The stock solution of each probe (10 mM in DMSO) was diluted to the concentration of 10  $\mu$ M using DMSO for the following binding constant measurement.

Various amounts of probes **1-9** (10  $\mu$ M in DMSO) was added (final concentration to be 2.5 nM, 5.0 nM, 10.0 nM, 20.0 nM, 40.0 nM, 60.0 nM, 100.0 nM and 150.0 nM) into 2.0 mL PBS buffer (pH = 7.4) containing 2.5  $\mu$ M A $\beta$  monomers, oligomers or aggregates respectively. After being mixed with pipette, the fluorescence spectrum of solution was recorded using a HORIBA Jobin Yvon Fluoromax-4 fluorometer. The K<sub>d</sub> value of each probe against different A $\beta$  species was calculated based on the fluorescence enhancement ( $\Delta FI = F_{(C(A\beta))} - F_0$ , where F<sub>0</sub> is the fluorescence intensity of A $\beta$  species without probes, and F<sub>(C(A $\beta$ ))</sub> is the fluorescence intensity of A $\beta$  species upon addition with a tested concentration of probe). The K<sub>d</sub> binding curve was generated using Prism 5.0 software with nonlinear one-site binding regression.

## LogP measurement

First, the standard curve of each probe was obtained for the following quantification. Second, probe **1-9** (0.1 mM) in 1.0 mL octanol with was subjected to partition with 1.0 mL octanol-saturated water. The resulting mixture was stirred vigorously for 5 min, and centrifuged at 3,000 rpm for 5 min. The

octanol layer was separated from water layer, and its fluorescence spectrum was recorded. The concentration of each probe in octanol layer was calculated using the equation generated from its standard curve. The concentration in water layer was deduced by subtracting the amount of each probe in octanol layer from its total added amount. The logP value was calculated by the ratio of each probe's concentration in octanol layer and water layer respectively.

## Cell culture

U87MG glioblastoma cells and PC-12 cells were purchased from Stem Cell Bank, Chinese Academy of Sciences (Shanghai, China). U87MG glioblastoma cells were grown in high glucose Dulbecco's modified Eagle's medium (DMEM) (Gibco) containing 10% fetal bovine serum (FBS) (Gibco), and 1% penicillin/streptomycin (Gibco) and cultured in a 5% CO<sub>2</sub> humidified incubator at 37 °C. PC-12 cells were cultured in Roswell Park Memorial Institute 1640 medium (RPMI-1640) supplemented with 10% fetal bovine serum (FBS) (Gibco), and 1% penicillin/streptomycin (Gibco) and cultured in a 5% CO<sub>2</sub> humidified incubator at 37 °C.

## Cytotoxicity studies

U87MG cells were seeded on flat-bottomed 96-well plates (5000 cells/well) and incubated at 37 °C for 24 h. Varying concentrations of probe **2** or probe **9** (0, 0.25, 0.5, 1.0, 2.5, 5.0, 10  $\mu$ M) in the DMEM medium were then added. After being incubation for 24 h, 50  $\mu$ L MTT solution (1 mg/mL in PBS) was added into each well. The cells were kept at 37 °C for another 4 h, and the medium in each well was then removed carefully. The resulting purple crystals in the wells were dissolved by addition of 150  $\mu$ L DMSO. The absorbance (OD) of formazan at 490 nm in each well was recorded on a microplate reader (Tcan). The absorbance of cells without any treatment (OD<sub>control</sub>) were used as the control, and the percentage of cell viability in each treatment was calculated by dividing OD to OD<sub>control</sub>. Every experiment was repeated three times.

The cytotoxicity of probe **2** and probe **9** towards PC-12 cells were performed by adopting the same way except that the medium was changed with 1640 medium.

## Animal Models

Normal ICR mice (5 weeks, male) and BALB/c mice (5 weeks, female) were purchased from the Model Animal Research Center (MARC) of Nanjing University (Nanjing, China). Transgenic mice (C57BL6, APP<sup>swe</sup>/PSEN1, 4–14 months old, male), used as Alzheimer's models, and its littermates were

also purchased from the Model Animal Research Center (MARC) of Nanjing University (Nanjing, China). All animal experiments were approved by the Institutional Animal Care and Use Committee (IACUC) of Nanjing University.

### Detection of exogenous A $\beta$ species in mouse brain homogenates

A 5-week old ICR mouse was sacrificed. The brain was dissected and homogenized with 2.0 mL PBS buffer (pH = 7.4). 0.1 mL of the resultant homogenate was added to a 96-well plate, followed by the addition of probe **2** (5  $\mu$ M of final concentration) and the A $\beta$  monomers, oligomers and aggregates (5  $\mu$ M of final concentration). Then the resulting brain homogenates were recorded using an IVIS Lumina XR III animal imaging system (Caliper LifeSciences, PerkinElmer). The parameter is  $E_x/E_m = 620 \text{ nm}/710 \text{ nm}$ .

### In vitro fluorescent staining of brain slice

Paraffin-embedded 10  $\mu$ m brain tissue sections from APP/PS1 transgenic mouse (C57BL6, APP/PS1, 14 months old, male) and age-matched wild-type mice (C57BL6, 14 months old, male) were used for *in vitro* fluorescent staining. Before staining, the slices were deparaffinized by washing with ethanol for 5 min after 15 min immersion in xylene. After washing with 50% ethanol, DD water and PBS buffer (pH = 7.4) respectively, the slices were incubated in aqueous solution of each probe (10  $\mu$ M) for 20 min at room temperature and then washed with ethanol/water (v/v = 50%:50%) followed by washing with PBS buffer (pH = 7.4). After removing the residual liquid with dust free paper, the slice was co-stained with 1% Thioflavin T (30% ethanol solution) for 10 min. Next, the slice was covered with VectaShield mounting media. Florescence images were observed using Olympus VS200 microscope.

### In vivo NIR fluorescence imaging

*In vivo* NIR fluorescence imaging was performed using IVIS Lumina XR III animal imaging system (Caliper LifeSciences, PerkinElmer). Images for probes **2**, **4** and **9** were acquired with a 620 nm excitation filter and a 710 nm emission filter. Images for probe **6** were acquired with a 600 nm excitation filter and a 710 nm emission filter. Images for CRANAD-58 were acquired with a 580 nm excitation filter and a 670 nm emission filter. Data analysis was performed using Living Image Software (4.5.2, PerkinElmer, MA, U.S.A.). The heads of 10 months old mice (male transgenic APP/PS1, n = 3 and age-matched male wild-type control mice, n = 3) were shaved before background imaging. The solutions of probe **2**, **4**, **6**, **9** and CRANAD-58 (1.0 mg/kg) were

freshly prepared in 20% DMSO, 20% cremorphor, and 60% PBS buffer (pH = 7.4), and the solutions were stabilized for 20 min before i.v. injection into mice. Fluorescence signals from the brain were recorded before and at 10, 30, 60, 120, 240 and 360 min after intravenous injection of the probes. To evaluate the imaging results, a region of interest (ROI) was drawn around the brain region. Intensity of brain fluorescence was calculated from the radiant efficiency. Note: For different probes, the mice in its corresponding groups (e.g. APP/PS1 mice group or age-matched control mice group) might be used repeatedly.

The *in vivo* NIR fluorescence imaging with probe **9** in 6-month-old APP/PS1 mice and age-matched control mice was conducted in the same way.

### Thinning skull surgery

The APP/PS1 mouse or age-matched control mouse (14 months old) was anesthetized with a solution of Midazolam (5.0 mg/kg), and Medetomidine (0.5 mg/kg), and a thin-skull imaging window was surgically prepared according to previously reported approach [40].

### Upright fluorescence microscopic imaging

Probe **9** (1.0 mg/kg in a fresh solution containing 20% cremorphor, 20% DMSO and 60% PBS buffer) was injected intravenously at time 0 min by a bolus injection during image acquisition. The fluorescence excitation was 615 nm (ANDOR, Sona). Imaging was performed using an upright microscope (Nikon technologies) equipped with a 4  $\times$  water immersion objective (Nikon NIR Apo). Images were collected every 5 seconds per frame 512 $\times$ 512  $\mu$ m matrix, and last for 20 min. Images were analyzed with ImageJ software.

### Statistical analysis

Statistical comparison between two groups was evaluated by Student's t-test. All the results were analyzed using Prism 7 (Prism GraphPad Software, Inc., San Diego). Results were expressed as mean  $\pm$  SD, and p < 0.05 was considered statistically significant.

## Results

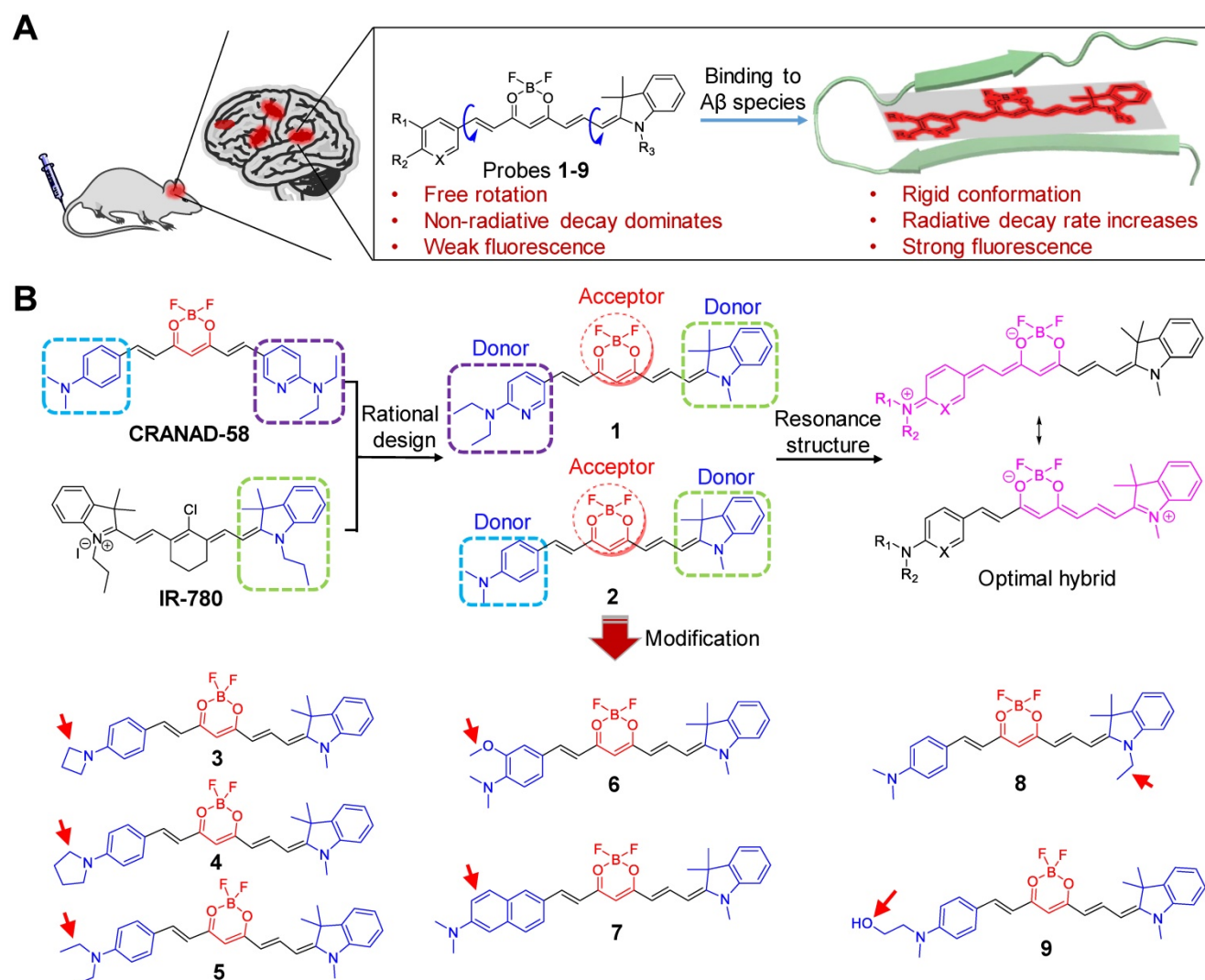
### Design and Synthesis of NIR Fluorescent probes for A $\beta$ species

Figure 1B illustrates the general design of the NIR fluorescent probes (**1** and **2**) on the basis of a D-A-D architecture by rationally hybridizing CRANAD-58 and IR-780, a widely used cyanine-based NIR fluorophore with the maximum fluorescence emission at 820 nm [41-44]. Considering

that the electron-donating ability of the indoline moiety in IR-780 was superior to that of either 4-*N,N'*-dimethylaminophenyl or 6-*N,N'*-diethylaminopyridyl group in CRANAD-58 [45], we envisioned that the presence of 1,3,3-trimethyl-indoline group in probes **1** and **2** could allow a more efficient delocalization of electrons through the  $\pi$  conjugated system, thereby contributing to longer absorption and emission wavelengths than that of CRANAD-58. After screening of probe **2** to be optimum over probe **1**, further modification of probe **2** was then conducted. First, to augment the bathochromic effect and improve binding affinity toward A $\beta$  species, probes **3-6** were designed by substituting the 4-*N,N'*-dimethylaminophenyl moiety with other stronger electron-donating groups, such as 4-azetidinyphenyl, 4-pyrrolidinylphenyl ring, 4-*N,N'*-diethylaminophenyl group, and 3-methoxyl-4-*N,N'*-dimethylaminophenyl group [46]. Second, to elongate the  $\pi$  conjugation for red-shifting

fluorescence emission, we designed probe **7** with a 6-*N,N'*-dimethyaminonaphthyl group in placing the 4-*N,N'*-diethylaminophenyl group of probe **2**. Third, to examine the steric effect of indoline on detecting A $\beta$  species, probe **8** was designed by replacing the 1,3,3-trimethyl-indoline group with *N*-ethyl-3,3-dimethyl-indoline group. Fourth, to optimize the physiological properties for improving fluorescence imaging of A $\beta$  species *in vivo*, probe **9** was designed with introduction of an *N*-methyl-*N'*-hydroxyethyl group [25, 47].

Probes **1-9** were synthesized according to the protocol outlined in Scheme S1. Condensation of 2,2-difluoro-1,3-dioxaboryl-pentadione (**A1**) with substituted aromatic aldehyde (**B1-8**) in the presence of acetic acid and tetrahydroisoquinoline afforded intermediates (**C1-8**). The subsequent condensation with Fischer's aldehyde **D1** or **D2** in acetic anhydride yielded the desired probes **1-9** as dark blue solids with purity >97% (Figure S1).



**Figure 1.** (A) The proposed mechanism for *in vivo* imaging of A $\beta$  species via binding-induced fluorescence “turn on”. (B) Design of NIR fluorescent probes **1** and **2** by hybridizing CRANAD-58 and NIR-780, and chemical modification of probe **2** into probes **3-9**.

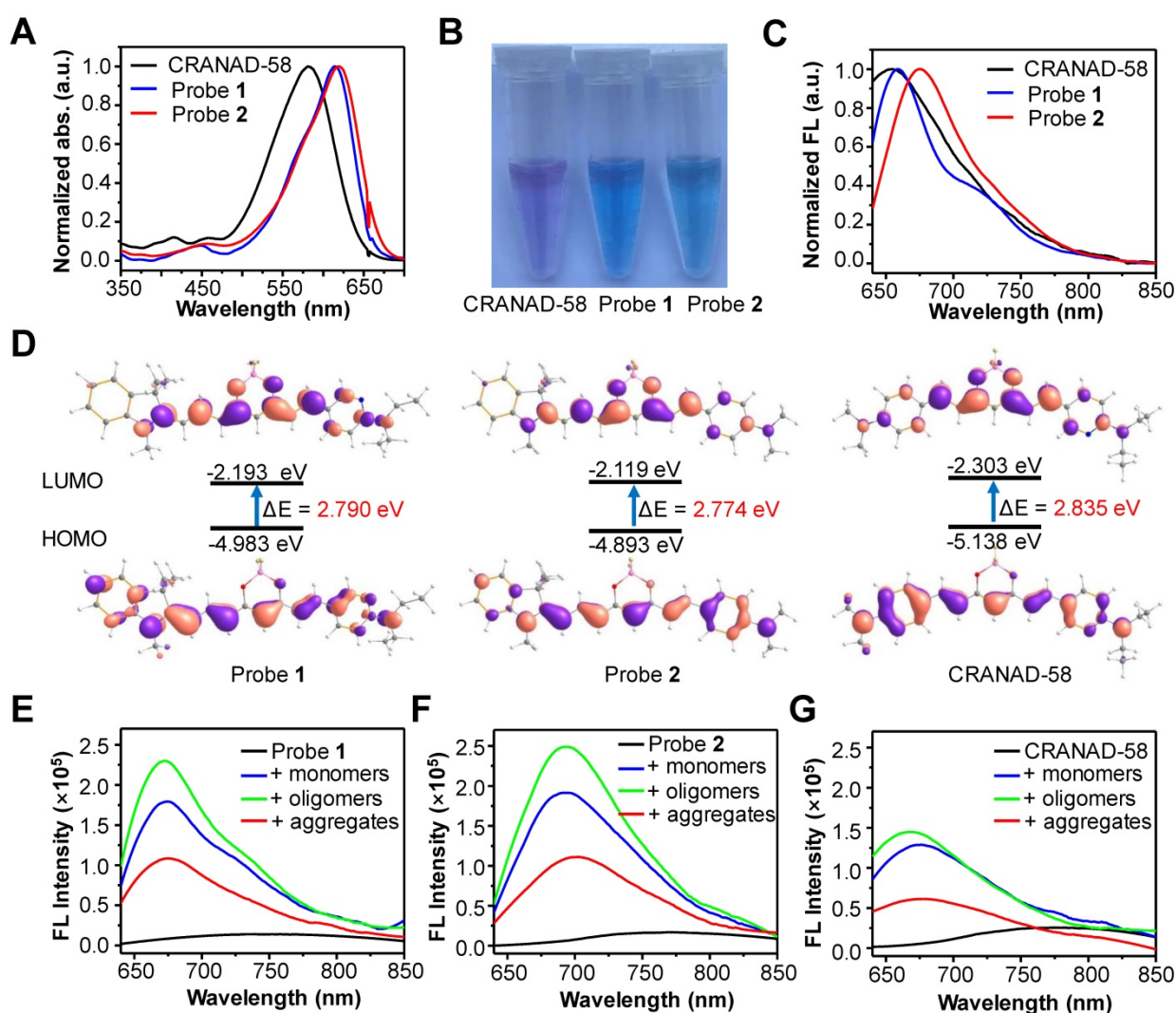


**Figure 2.** (A) Normalized UV-vis absorption (abs.), (B) photograph and (C) normalized fluorescence (FL) spectra of CRANAD-58, probes 1 and 2 in  $\text{CH}_2\text{Cl}_2$ . (D) Frontier molecular orbitals of the HOMO and LUMO of CRANAD-58, probe 1 and 2. The energy gap between HOMO and LUMO decreased at an order of probe 2, probe 1 and CRANAD-58. (E, F, G) FL spectra of probe 1 (E), probe 2 (F) or CRANAD-58 (G) upon incubation with 250 nM  $\text{A}\beta_{42}$  monomers,  $\text{A}\beta_{42}$  oligomers and  $\text{A}\beta_{42}$  aggregates in PBS buffer, respectively. The concentration of each probe is 250 nM.

### Investigation of photophysical properties of probes 1 and 2

We first investigated the optical properties of probes 1 and 2. As shown in Figure 2A, the maximum UV-vis absorbance of probes 1 and 2 in  $\text{CH}_2\text{Cl}_2$  was found to be 614 nm and 619 nm, respectively, which were more than 30 nm longer than that of CRANAD-58 ( $\lambda_{\text{abs}} = 581$  nm). Owing to the bathochromic shift in UV-vis absorption, both probes 1 and 2 displayed a blue color in  $\text{CH}_2\text{Cl}_2$ , whereas CRANAD-58 showed a purple color (Figure 2B). The fluorescence emission of probe 2 in  $\text{CH}_2\text{Cl}_2$  appeared in the NIR region ( $\lambda_{\text{em}} = 675$  nm), which was longer than that of probe 1 ( $\lambda_{\text{em}} = 659$  nm) and CRANAD-58 ( $\lambda_{\text{em}} = 653$  nm) (Figure 2C). These results demonstrate that probe 2 containing the 1,3,3-trimethyl-indoline group displayed a more obvious bathochromic shift in fluorescence emission compared with probe 1 or

CRANAD-58, according with their HOMO-LUMO gaps theoretically calculated (Figure 2D). We then examined the fluorescence emissions of probes 1 and 2 in solvent with different polarity. As expected, their fluorescence was very weak in aqueous solution (e.g. PBS buffer), which shifted blue with fluorescence intensity remarkably increased when the polarity of solvent decreased, similar to that of CRANAD-58 (Figure S2). The subsequent measurement of the absolute quantum yields ( $\Phi_f$ ) showed that the  $\Phi_f$  value of probe 2 was  $\sim 26.3\%$  in  $\text{CH}_2\text{Cl}_2$ , higher than that of probe 1 ( $\sim 13.2\%$ ) or CRANAD-58 ( $\sim 9.6\%$ ), whereas the  $\Phi_f$  values of them in PBS buffer were all less than 0.1% (Table S1). As  $\text{CH}_2\text{Cl}_2$  is a typical solvent to mimic the hydrophobic “binding pocket” of the  $\text{A}\beta$  species [48], we envisioned that such dramatic different  $\Phi_f$  values between  $\text{CH}_2\text{Cl}_2$  and PBS buffer might endow probes 1 and 2 “off-on” NIR fluorescence toward  $\text{A}\beta$  species.

**Table 1.** Response of probe **1-9** toward A $\beta$  monomers, oligomers and aggregates in PBS buffer

Probes	A $\beta$ monomers			A $\beta$ oligomers				A $\beta$ aggregates				
	$\lambda_{ex}$ (nm)	$\lambda_{em}$ (nm)	fold <sup>a</sup>	$K_d$ (nM)	$\lambda_{ex}$ (nm)	$\lambda_{em}$ (nm)	fold <sup>a</sup>	$K_d$ (nM)	$\lambda_{ex}$ (nm)	$\lambda_{em}$ (nm)	fold <sup>a</sup>	$K_d$ (nM)
<b>1</b>	616	674	26	4.00 $\pm$ 0.34	615	672	29	35.66 $\pm$ 2.39	619	675	13	15.38 $\pm$ 1.07
<b>2</b>	620	693	34	8.64 $\pm$ 0.37	619	692	44	67.83 $\pm$ 4.70	620	700	15	28.02 $\pm$ 2.00
<b>3</b>	617	697	46	10.64 $\pm$ 1.03	618	695	53	36.16 $\pm$ 1.68	621	705	13	13.78 $\pm$ 1.06
<b>4</b>	623	702	51	31.66 $\pm$ 2.31	620	696	74	186.8 $\pm$ 22.69	623	708	20	39.93 $\pm$ 3.63
<b>5</b>	623	701	20	15.57 $\pm$ 1.74	619	694	30	72.57 $\pm$ 5.75	622	706	9	54.15 $\pm$ 4.15
<b>6</b>	593	707	15	3.01 $\pm$ 0.41	591	702	22	25.62 $\pm$ 1.54	605	705	9	13.51 $\pm$ 0.73
<b>7</b>	618	700	36	64.20 $\pm$ 5.38	615	692	43	166.8 $\pm$ 19.91	610	718	6	142.1 $\pm$ 8.29
<b>8</b>	616	692	42	10.14 $\pm$ 0.74	620	690	71	118.6 $\pm$ 9.71	622	700	23	76.34 $\pm$ 5.65
<b>9</b>	617	690	28	11.16 $\pm$ 0.79	618	688	35	36.59 $\pm$ 2.69	620	697	10	14.57 $\pm$ 1.27
CRANAD-58	580	674	27	4.84 $\pm$ 0.47	584	667	39	32.66 $\pm$ 1.99	588	675	12	13.49 $\pm$ 0.84

<sup>a</sup> Fluorescence activation ratio (fold) was measured by incubating 250 nM probe with 250 nM A $\beta$  species.

We next tested the fluorescence response of probes **1** and **2** toward both soluble A $\beta$  species (A $\beta_{42}$  monomers and A $\beta_{42}$  oligomers) and insoluble A $\beta$  species (A $\beta_{42}$  aggregates). Akin to CRANAD-58, both probes **1** and **2** displayed weak fluorescence in PBS buffer alone; upon binding to A $\beta$  species, a significant enhancement in fluorescence intensity together with a blue shift in fluorescence emission occurred (Figure 2E-G). There were significantly ~34-fold, ~44-fold and ~15-fold increments in fluorescence intensity upon binding of probe **2** (250 nM) with one equivalent of A $\beta_{42}$  monomers, oligomers and aggregates, respectively, larger than that of probe **1** or CRANAD-58 (Table 1). Moreover, upon interaction with the A $\beta_{42}$  species, the fluorescence wavelengths of probe **2** appeared at 693 nm for A $\beta$  monomers, 692 nm for A $\beta$  oligomers, and 700 nm for A $\beta$  aggregates, which were also revealed from the contour maps of fluorescence spectra (Figure S3). All the fluorescence wavelengths were longer than that CRANAD-58 upon binding with A $\beta$  monomers ( $\lambda_{em}$  = 674 nm), A $\beta$  oligomers ( $\lambda_{em}$  = 667 nm), or A $\beta$  aggregates ( $\lambda_{em}$  = 675 nm). In contrast, the fluorescence wavelengths of probe **1** after binding with the A $\beta_{42}$  species were all much shorter than that of probe **2**, which could be presumably owing to the reduced electron-donating ability of 6-*N,N'*-diethylaminopyridyl in probe **1** compared with that of 4-*N,N'*-dimethylaminophenyl group in probe **2**, thus weakening the bathochromic effect. These findings accorded with the aforementioned fluorescence emission in CH<sub>2</sub>Cl<sub>2</sub> (Figure 2C). The examination of binding affinity against A $\beta$  species showed that both probes **1** and **2** could bind strongly with all the A $\beta$  species, with  $K_d$  values at a nM level, similar to that of CRANAD-58 (Figure S4-6 and Table 1). Considering the longer emission wavelengths and higher fluorescence “turn-on” ratios upon binding with A $\beta$  species, probe **2** deemed to be optimum over probe **1** and CRANAD-58 for subsequent fluorescence imaging of A $\beta$  species.

### Detection of A $\beta$ species with probe **2** *in vitro*

We then chose probe **2** as the optimum to investigate the ability to detect A $\beta$  species *in vitro*. First, we measured the binding kinetics of probe **2** against A $\beta$  monomers, oligomers and aggregates. As shown in Figure 3A, the fluorescence intensity of probe **2** (250 nM) immediately increased upon mixing with each A $\beta$  species (250 nM), which could reach the plateau within 10 s for A $\beta$  monomers and A $\beta$  oligomers, and about 150 s for A $\beta$  aggregates, indicating that the binding of probe **2** with the A $\beta$  species was kinetically fast. Second, the limit of detection (LOD) of probe **2** toward different A $\beta$  species was determined by measuring the fluorescence spectra of probe **2** (250 nM) after being incubated with varying concentrations of A $\beta$  species (0-15  $\mu$ M) (Figure 3B and Figure S7). As shown in Figure 3B, the fluorescence intensity of probe **2** could linearly correlate with A $\beta$  monomers, oligomers and aggregates at a concentration range of 100 nM-6.4  $\mu$ M, 50 nM-3.2  $\mu$ M and 100 nM-10  $\mu$ M, respectively. The LOD ( $3\sigma/k$ ) was then calculated to be ~14.1, ~12.8 and ~12.9 nM for the monomers, oligomers and aggregates, respectively, which were comparable to that of other previously reported fluorescent probes for A $\beta$  aggregates [28, 49-53]. Third, the examination of the selectivity toward the A $\beta$  proteins over other representative endogenous species, including L-Cysteine, glutathione, vitamin C, Cytochrome C, BSA, AChE, BuChE, Amylin, hMAO-A,  $\beta$ -Galactosidase, and reactive oxygen species (hydroxyl radical, singlet oxygen, superoxide radical, and H<sub>2</sub>O<sub>2</sub>) showed that strong fluorescence could be observed only in the presence of A $\beta$  monomers, oligomers or aggregates; negligible fluorescence appeared toward other examined species, especially Amylin or BSA, which were found to be notorious species potentially competing with the A $\beta$  species in the brain (Figure 3C). These results suggest that probe **2** hold high kinetics, sensitivity and specificity to detect both soluble and insoluble A $\beta$  species. Moreover, the

confocal fluorescence microscopy imaging of A $\beta$  oligomers or aggregates stained with probe 2 showed the occurrence of bright NIR fluorescence, which could clearly delineate the different morphology of A $\beta$  oligomers and aggregates, confirming the good ability for fluorescence imaging of A $\beta$  species (Figure S8).

To further gain insights into the binding sites between probe 2 and A $\beta$  species, three different experiments were then carried out. First, competition assay by titrating probe 2 against ThT (250 nM, a gold standard agent for the A $\beta$  plaques) bound A $\beta_{42}$  fibrillar aggregates (2.5  $\mu$ M) showed that the fluorescence of ThT at 482 nm decreased and nearly returned to the background upon gradual addition of probe 2, while the fluorescence of probe 2 at  $\sim$ 700 nm increased concurrently, suggesting effective displacement of ThT from the A $\beta_{42}$  aggregates by probe 2 (Figure 3D). By contrast, a reverse competition test by titrating ThT against probe 2 (250 nM) bound A $\beta_{42}$  fibrillar aggregates (2.5  $\mu$ M) showed that the strong NIR fluorescence of probe 2 was kept, while the

fluorescence of ThT was negligibly enhanced, suggesting ineffective displacement of probe 2 from the A $\beta_{42}$  aggregates by ThT (Figure 3E). These findings imply that (1) probe 2 and ThT could probably bind to the same sites in the A $\beta_{42}$  aggregates, and (2) probe 2 showed a much higher binding affinity than that of ThT toward the A $\beta_{42}$  aggregates. Second, we investigated whether probe 2 could bind with the A $\beta_{16-20}$  segment (KLVFF) and induce fluorescence enhancement as it has been previously reported that the KLVFF sequence was the major hydrophobic fragment for ThT binding. After incubating probe 2 (250 nM) with the KLVFF peptide (250 nM) in a PBS buffer, the fluorescence of probe 2 blue shifted to  $\sim$ 700 nm and the intensity increased about 4.4-fold, while the incubation of probe 2 with the KLVFF free segment A $\beta_{22-35}$  (EDVGSNKGAIIGLM) showed neither blue shift nor intensity enhancement in fluorescence, suggesting that the KLVFF fragment was probably the core site for probe 2 binding (Figure 3F). Third,  $^1$ H-NMR spectroscopy showed obvious changes in the chemical

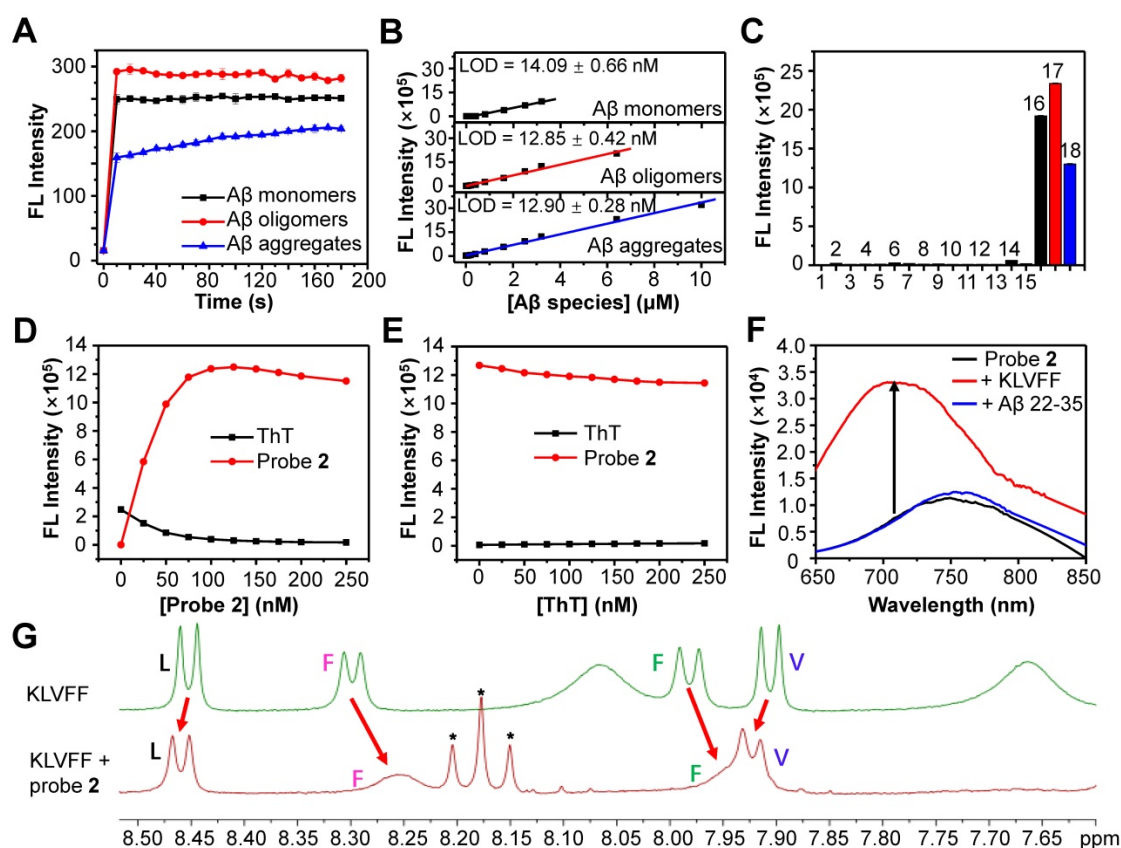


**Figure 3.** (A) FL intensity ( $\lambda_{exc/em}$ =620/700 nm) of probe 2 (250 nM) following incubation with 250 nM A $\beta_{42}$  monomers (black), oligomers (red) and aggregates (blue) for 0–180 s. (B) Plots of the mean FL intensity of probe 2 (250 nM) versus varying concentration of A $\beta_{42}$  monomers (black), oligomers (red) and aggregates (blue). (C) FL intensity of 250 nM probe 2 upon incubation with A $\beta_{42}$  species (10  $\mu$ g/ml) and other representative endogenous biological species (10  $\mu$ g/ml) in PBS buffer (1: PBS, 2: OH $\cdot$  (200  $\mu$ M Fe $^{2+}$  + 1 mM H $_2$ O $_2$ ), 3:  $^1$ O $_2$  (1 mM H $_2$ O $_2$  + 1 mM ClO $_2$ ), 4: O $_2^{\cdot-}$  (100  $\mu$ M xanthine + 22 mU xanthine oxidase), 5: H $_2$ O $_2$  (1 mM H $_2$ O $_2$ ), 6: hMAO-A, 7:  $\beta$ -Galactosidase, 8: AChE, 9: BuChE, 10: L-Cysteine, 11: GSH, 12: Cytochrome C, 13: Vitamin C, 14: Amylin, 15: BSA, 16: A $\beta_{42}$  monomers, 17: A $\beta_{42}$  oligomers, 18: A $\beta_{42}$  aggregates). (D, E) Change in the FL intensities of ThT ( $\lambda_{exc/em}$  = 445/482 nm) and probe 2 ( $\lambda_{exc/em}$  = 620/700 nm) upon titrating (D) probe 2 to ThT-A $\beta_{42}$  aggregates mixture or (E) ThT to probe 2-A $\beta_{42}$  aggregates mixture in PBS buffer. (F) FL spectra of probe 2 (black) and probe 2 (250 nM) incubating with KLVFF (250 nM) or A $\beta_{22-35}$  (250 nM) peptides. (G) Comparison of the  $^1$ H-NMR spectra (DMSO- $d_6$ , 500 MHz) of KLVFF (2.0 mM) in the presence (red) or absence (green) of probe 2 (2.0 mM). Red arrows indicated the change of chemical shifts of the amide protons of L, V and F residues. \* indicating the  $^1$ H-NMR peaks from probe 2.

shifts of amide protons of L, V and F residues in the solution containing probe **2** and KLVFF peptide, supporting the interaction of probe **2** with the hydrophobic KLVFF peptide fragment (Figure 3G). We envisioned that the insertion of probe **2** into the hydrophobic site of A $\beta$  proteins could help to restrain double-bond rotation and increase radiative decay rate of probe **2** after excitation, consequently enhancing fluorescence emission. This phenomenon was further validated by the obvious blue-shift and enhancement in fluorescence emission of probe **2** when the solvent viscosity increased (Figure S9). In all, these results revealed that the KLVFF core fragment was likely the key site for the interaction between probe **2** and the A $\beta$  species, effectively switching on the NIR fluorescence of probe **2**.

To examine the ability of probe **2** for the fluorescence imaging of endogenous A $\beta$  species in biological environment, we first demonstrated that probe **2** hold good stability in PBS buffer (Figure S10), mouse serum (Figure S11) and good photostability under continuous irradiation of lamplight (Figure S12). Next, the biocompatibility of probe **2** was examined to show negligible cytotoxicity against human glioma U87MG cells and PC-12 cells after being incubated with probe **2** at 10  $\mu$ M for 24 h (Figure S13). Furthermore, we investigated the ability of the probe to detect exogenous A $\beta$  species in mouse brain homogenates via fluorescence imaging. As shown in Figure S14, mouse brain homogenates containing 5  $\mu$ M A $\beta$  monomers, A $\beta$  oligomers or A $\beta$  aggregates displayed much brighter NIR fluorescence images compared to that of native mouse brain homogenates

after its incubation with probe **2** (5  $\mu$ M), indicating that probe **2** could well detect the exogenous A $\beta$  species in brain homogenates.

### NIR fluorescence imaging of A $\beta$ species *in vivo*

Having demonstrated the good capacity of probe **2** for the detection of exogenous A $\beta$  species, we then applied probe **2** to detect endogenous A $\beta$  species via NIR fluorescence imaging. First, the log*P* values of probe **2** was measured, which was found to be  $\sim 2.31$ , ensuring a proper lipophilicity to cross the BBB and enter brain (Table S1). Then, probe **2** or CRANAD-58 (1.0 mg/kg) was intravenously (i.v.) injected into three 10-month-old male APP/PS1 double transgenic mice (APP/PS1) and three age-matched WT mice, and fluorescence images of mouse brain were longitudinally acquired. As shown in Figure 4A (More imaging details are shown in Figure S15 and Figure S16), bright fluorescence appeared in the brain of APP/PS1 mice at 10 min post injection of probe **2** or CRANAD-58, and the fluorescence intensity maximized at 30 min, which then decreased thereafter. APP/PS1 mice showed significantly brighter brain fluorescence images than that of WT mice; the average fluorescence intensity was  $\sim 1.3$ -fold higher in the APP/PS1 mice brains than that of WT mice at 10 min post injection of probe **2**, which increased to  $\sim 1.5$ -fold at 30 min and  $\sim 2.0$ -fold after 4-6 h (Figure 4B). It was also found that the brain fluorescence in probe **2**-treated APP/PS1 mice was much brighter than that in mice following i.v. injection of a same dosage of CRANAD-58 (1.0 mg/kg), presumably owing to that probe **2** possesses

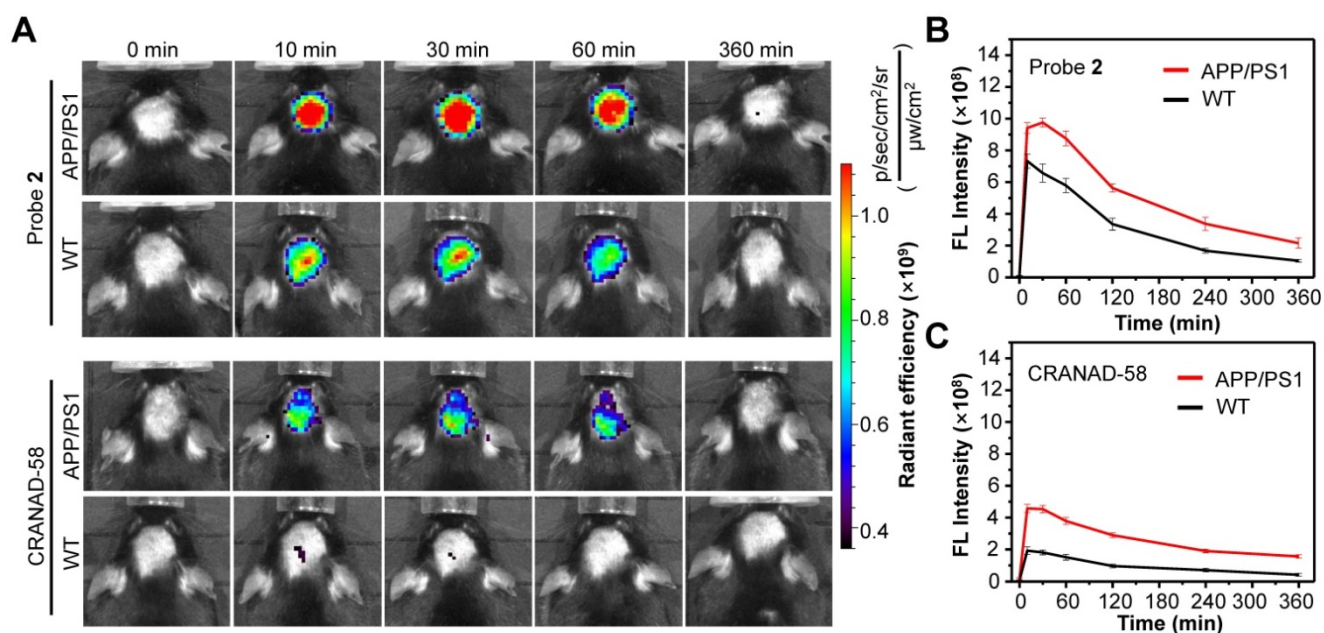


**Figure 4.** Longitudinal NIR FL images (A) and mean brain FL intensities of APP/PS1 transgenic mice and WT mice (10-month old) following i.v. injection of probe **2** (B) and CRANAD-58 (C) (1.0 mg/kg) at 0, 10, 30, 60, and 360 min. Data are mean  $\pm$  standard deviation (S.D.) (n = 3).

longer fluorescence emission and higher  $\Phi_f$  value in relative to CRANAD-58 (Table S1), which could enhance penetration depth and improve sensitivity for *in vivo* imaging. However, compared to probe 2, CRANAD-58 also produced darker brain fluorescence in the WT mice; thereby, the brain fluorescence intensity in the APP/PS1 mice was also significantly higher than that in WT mice (Figure 4C), consistent to the results reported by Ran [18]. These findings indicate that probe 2 could readily cross the BBB and produce strong NIR fluorescence to differentiate APP/PS1 AD mice from WT mice after i.v. injection into mice, which was similar to CRANAD-58.

To validate whether the enhanced brain fluorescence in APP/PS1 mice was due to the binding of probe 2 to the upregulated A $\beta$  species, the brains of 14-month-old APP/PS1 and WT mice were resected 30 min after probe 2 injection, and the brain tissue slices were then cut and co-stained with ThT. Fluorescence imaging of the brain tissue slices showed that bright fluorescent dots appeared both in hippocampus and cerebral cortex of the APP/PS1 mouse brain tissue slices, which colocalized well with the fluorescence of ThT (Figure 5A), whereas no similar fluorescent dots could be found in the WT

group (Figure S17). Additionally, intensive fluorescent dots could also be observed in the cerebellum area from the APP/PS1 mouse (Figure 5B), not from the WT mouse (Figure S18). These results confirmed that probe 2 could selectively stain the endogenous A $\beta$  plaques, thus lighting up the AD mouse brain. Note that the green fluorescence of ThT was largely located in the core of the plaques where the A $\beta$  aggregates deposit, whereas the enhanced fluorescence of probe 2 appeared both in the core and the peripheral areas of the A $\beta$  plaques where the A $\beta$  oligomers are likely resided. These findings suggest that probe 2 could well label the endogenous A $\beta$  aggregates and A $\beta$  oligomers in the A $\beta$  plaques, which was advantageous over ThT. Moreover, we found that probe 2 could also efficiently highlight the cerebral amyloid angiopathies (CAAs) (Enlarged box 4 in Figure 5B), which is characterized by depositing A $\beta$  species at the exterior of brain arteries and is closely related with pathological dementia [38, 54]. To further verified the staining of CAAs, another 10-month-old APP/PS1 mouse and age-matched WT mouse was i.v. injected with probe 2 respectively. The brain of each mouse was resected at 30 min post injection and then cut into brain slice, which was

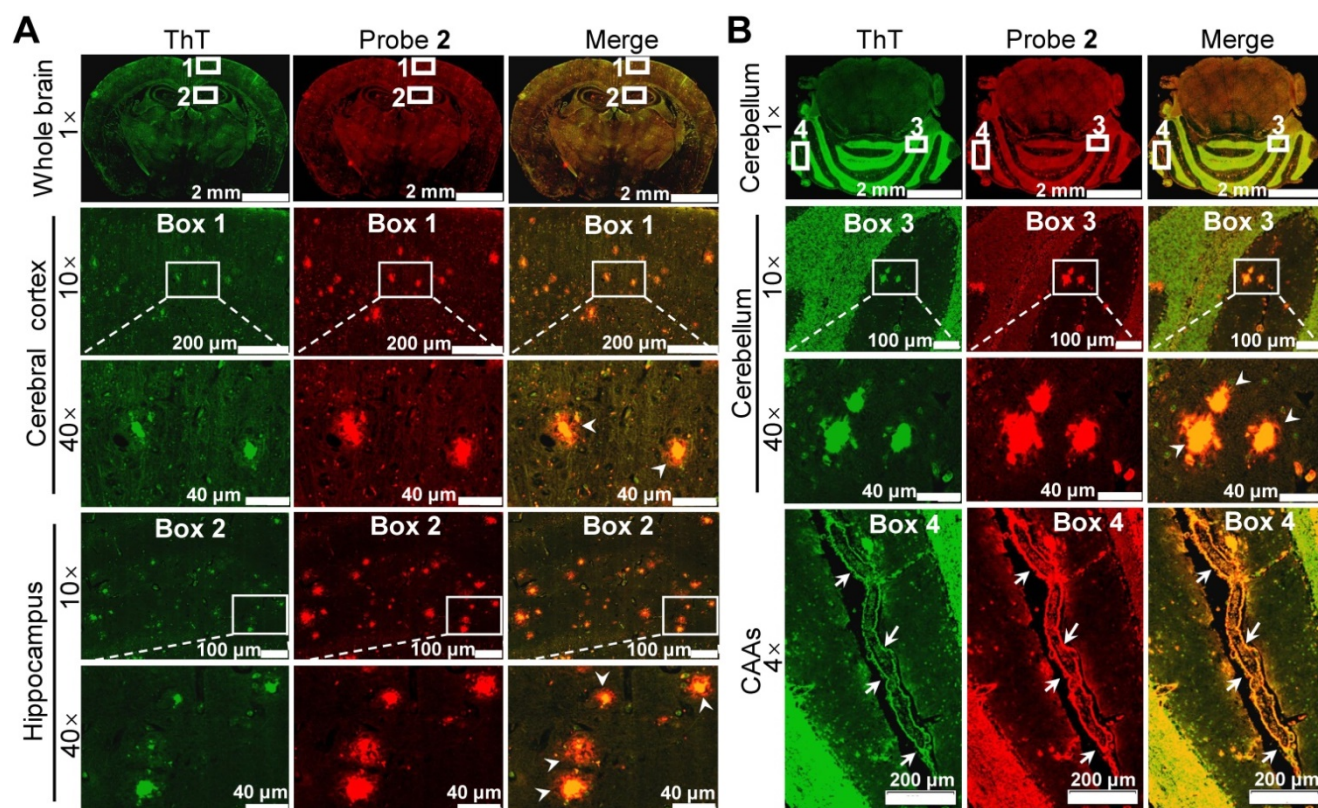


**Figure 5.** Ex vivo histological staining of the (A) cerebrum and (B) cerebellum tissues slices resected from an APP/PS1 mouse at 30 min after i.v. injection of probe 2 (1 mg/kg). The A $\beta$  plaques in both brain tissue slices were further confirmed by staining with ThT (green). Boxes 1 and 2 in figure (A) indicated enlarged cerebral cortex and hippocampus, respectively; boxes 3 and 4 in figure (B) indicated enlarged cerebellar corpus and CAAs. The white arrowheads showed that the enhanced fluorescence of probe 2 appeared both in the core and the peripheral areas of the A $\beta$  plaques in both cerebrum and cerebellum tissues. White arrows in enlarged box 4 showed the presence of CAAs in the cerebral vessels.

co-stained with ThT and AlexaFluor 488-labeled CD31 antibody respectively. As can be seen in Figure S19A, probe **2** could clearly light up the plaques distributed in the walls of brain vessels, while there were no fluorescent spots observed in WT mouse (Figure S19B). Taking together, the *ex vivo* histological imaging could well support the *in vivo* fluorescence imaging results, demonstrating that probe **2** was applicable for the noninvasive fluorescence imaging of A $\beta$  species in APP/PS1 AD mice.

### Chemical modification of probe 2

Encouraged by the above results, further modification of probe **2** to obtain probes **3-9** was performed (Figure 1B), endeavoring to improve the photophysical and physiochemical properties for *in vivo* fluorescence imaging of A $\beta$  species. As shown in Figure S20 and Table S1, the absorbance and NIR fluorescence emission wavelengths of probes **3-9** in CH<sub>2</sub>Cl<sub>2</sub> were close to that of probe **2**. Among them, probe **6** with the 3-methoxy-4-*N,N'*-dimethylamino-phenyl group showed a much longer fluorescence emission wavelength ( $\lambda_{em} = 706$  nm) than that of probe **2** ( $\lambda_{em} = 675$  nm) in CH<sub>2</sub>Cl<sub>2</sub>. As with probe **2**, they all showed an obvious solvatochromic effect on fluorescence emission (Figure S21). The subsequent examination of the fluorescence response toward A $\beta$  species showed that their weak NIR fluorescence in PBS buffer could be remarkably switched on after binding with A $\beta$  monomers, A $\beta$  oligomers and A $\beta$  aggregates, respectively (Figure S22). Probe **4** with the 4-pyrrolidinylphenyl ring showed the highest fluorescence turn-on ratio toward A $\beta$  monomers (~51-fold at 702 nm) and A $\beta$  oligomers (~74-fold at 696 nm), and approximately ~20-fold enhanced fluorescence (708 nm) toward A $\beta$  aggregates among all these compounds (Table 1).

We then examined their binding affinity toward A $\beta$  monomers, A $\beta$  oligomers and A $\beta$  aggregates, respectively (Figure S23-29 and Table 1). The  $K_d$  values of them were mostly at the nM level, indicating that these probes hold good binding affinities toward A $\beta$  species. It was notable that probe **6** with a 3-methoxy group as the *H*-bond acceptor exhibited higher binding affinities toward A $\beta$  monomer ( $K_d = 3.01 \pm 0.41$  nM), A $\beta$  oligomer ( $K_d = 25.62 \pm 1.54$  nM) and A $\beta$  aggregates ( $K_d = 13.51 \pm 0.73$  nM) than those of probe **2**, presumably because that the introduction of an *H*-bond acceptor could facilitate to form hydrogen bond with the engaged A $\beta$  proteins. Similar results were also observed for probe **9**, where the introduction of a hydrophilic hydroxyethyl group could not only help to lower the log*P* value to 2.14, but also facilitate to act as an *H*-bond acceptor to increase binding affinity against A $\beta$  oligomers ( $K_d =$

$36.59 \pm 2.69$  nM) and A $\beta$  aggregates ( $K_d = 14.57 \pm 1.27$  nM) as compared with probe **2**. Additionally, probe **7** containing the 6-*N,N'*-dimethyaminonaphthyl group showed longer fluorescence wavelengths after binding with each A $\beta$  species in relation to that of probe **2** as a result of the elongated  $\pi$  conjugation system, however, the  $K_d$  values against the A $\beta$  species were higher than that of probe **2** (Table 1). These results suggest that the introduction of a bulky donor group could probably attenuate the binding affinity toward A $\beta$  species, which was also observed for probe **8** containing the *N*-ethyl-3,3-dimethyl-indoline group.

### In vivo test of probes 4, 6 and 9

On the basis of the *in vitro* results, we next chosen probe **4** with optimum fluorescence enhancement, probe **6** with the highest binding affinity against each A $\beta$  species, and probe **9** with the lowest log*P* value for *in vivo* studies, aiming to improve visualization of endogenous A $\beta$  species in living AD mice. First, *in vitro* fluorescence staining of resected brain tissue slices from APP/PS1 AD and WT mice showed that these three probes could well highlight the A $\beta$  plaques in the cerebral cortex and hippocampus of APP/PS1 mouse (Figure S30, S32 and S34), not in WT mouse (Figure S31, S33 and S35). Then, probes **4**, **6** and **9** were each i.v. injected into male APP/PS1 AD mice and age-matched WT mice, and the brain fluorescence images were acquired at 0, 10, 30, 60 and 360 min post injection. As with probe **2**, the APP/PS1 mice displayed much brighter brain fluorescence than that of WT mice at 10 min post injection of each probe (Figure 6, More imaging details are shown in Figure S36, S37 and S38), with average brain fluorescence intensity considerably higher than that from the age-matched WT mice, suggesting that these three probes could also cross the BBB and efficiently differentiate the APP/PS1 AD mice from WT mice (Figure 6). Among them, probe **4** displayed relatively weaker brain fluorescence both in APP/PS1 and WT mice. However, there was significant ~2.0-fold higher fluorescence intensity in the brain of APP/PS1 mice compared to that in the WT mice at 10 min, which increased to ~2.8-fold at 60 min and ~3.2-fold at 6 h. These differences in brain fluorescence between APP/PS1 and WT mice achieved by probe **4** were larger than that of probes **2**, **6** and **9**, presumably owing to that probe **4** hold much higher fluorescence turn-on ratios toward A $\beta$  species compared to the other probes (Table 1). It was found that though probe **6** displayed the best binding affinities against each A $\beta$  species, it took about 60 min to reach the maximum brain fluorescence both in APP/PS1 and WT mice, much longer than that of

probe 2 and 4 (~30 min for them). In addition, probe 6 also showed a slower washout in the brain compared to the other probes, resulting in a narrower discrepancy between APP/PS1 and WT mice. In contrast, probe 9 hold the fastest kinetics (~10 min) to achieve the maximum brain fluorescence signal in the APP/PS1 mice, and produced higher brain fluorescence intensity compared to probe 2 or CRANAD-58. Moreover, a significantly ~1.7-fold higher brain fluorescence intensity in APP/PS1 mice relative to that in WT mice had occurred at 10 min, which was higher than that achieved by probe 2 (~1.3-fold at 10 min). Such increases in both maximum brain fluorescence intensity and discrepancy between APP/PS1 and WT mice at early time point (e.g., 10 min) suggest that probe 9 could be advantage over probe 2 for fluorescence imaging of A $\beta$  species *in vivo*, presumably owing to the reduced log $P$  value that potentially improves the physicochemical properties and enhances brain uptake. In addition, Figure S39 illustrated that probe 9 also produced a significantly ~1.5 fold higher signal intensity in APP/PS1 mice to that of WT mice to detect soluble A $\beta$  species in 6-month-old APP/PS1 mice at 10 min. Importantly, probe 9 showed similar *in vitro* properties to that of

probe 2 (Figure S12, S40, S41 and S42). The isothermal titration calorimetry experiment [55, 56] illustrated that per one probe 9 bound with ~1.22 number A $\beta$  monomers, ~0.0623 number A $\beta$  oligomers and ~0.161 number A $\beta$  aggregates respectively (Figure S43). Furthermore, we examined the blood half-life ( $t_{1/2}$ ) of probe 9 to be ~13.1 min (Figure S44). The biodistribution studies suggested that probe 9 possessed high brain uptake (Figure S45) and was eliminated mainly via hepatobiliary system (Figure S46), which was validated by the primary fecal metabolic pathway (Figure S47). As shown in Figure S48 and Figure S49, probe 9 also showed a good biocompatibility *in vivo*.

### Dynamic fluorescence imaging of A $\beta$ plaques in mouse brain using probe 9

Taking the advantage of fast kinetics to produce bright brain fluorescence offered by probe 9 due to its improved physiological properties, dynamic visualization of A $\beta$  plaques in the brains of mice was then conducted on an upright microscope. Probe 9 (1.0 mg/kg) was i.v. injected into a skull-thinning 14-month-old APP/PS1 mouse and an age-matched WT mouse respectively, and the brain fluorescence

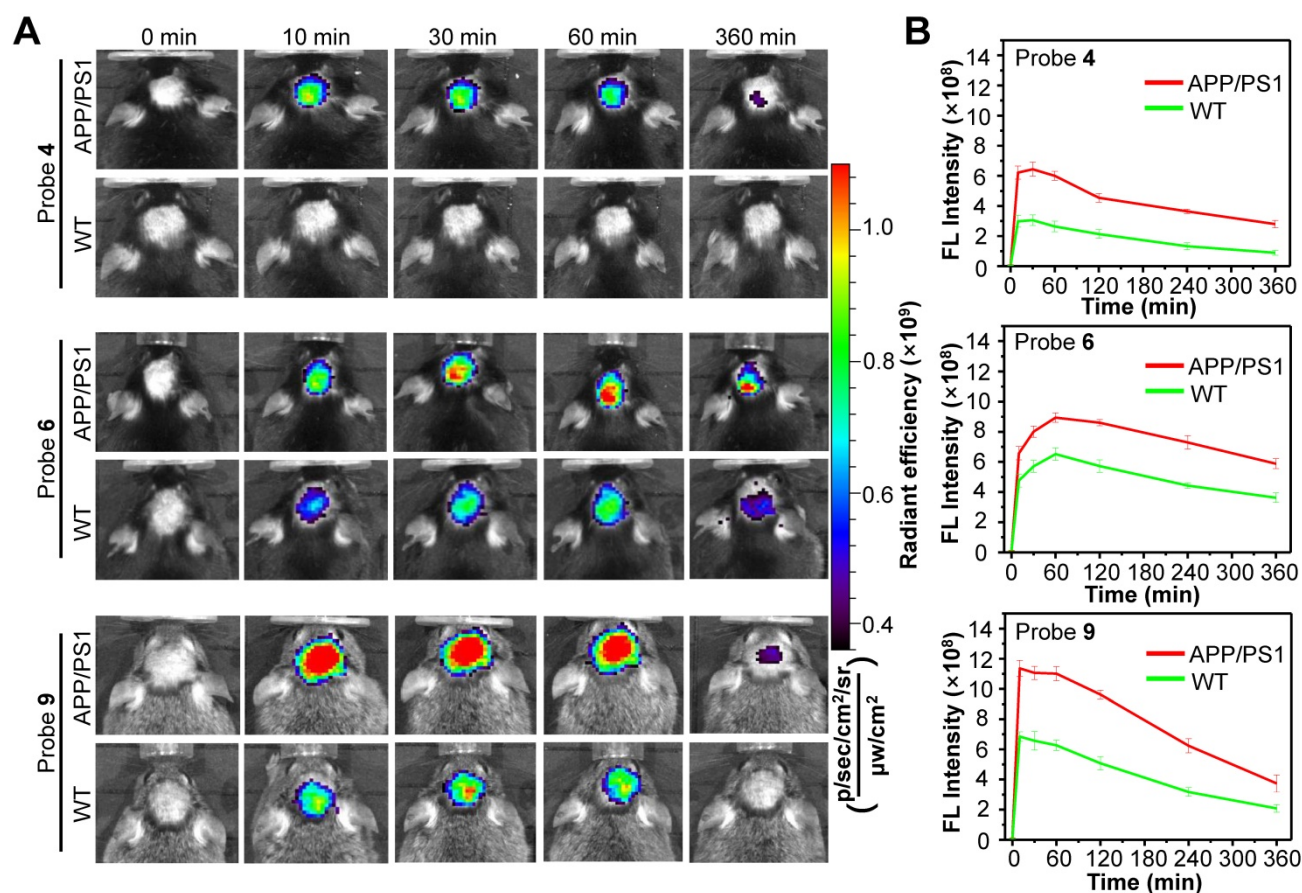


**Figure 6.** (A) Representative longitudinal FL images of APP/PS1 transgenic and WT mice (10-month old) following i.v. injection of probe 4, 6 or 9 (1.0 mg/kg) at 0, 10, 30, 60, and 360 min. (B) Quantitative analysis of the brain FL intensities of the APP/PS1 and WT mice at indicated time. Data are mean  $\pm$  S.D. (n = 3).

was sequentially acquired in the first 20 min. As shown in Figure 7 and the time-lapse movies (Movies S1 and 2), AD mouse brain showed bare autofluorescence in the NIR region before administration of probe 9; however, after injection of probe 9, bright NIR fluorescence could be immediately observed in the blood vessels and brain parenchyma of the APP/PS1 mouse, suggesting that probe 9 could rapidly cross the BBB and enter the parenchyma. Within 30 s, the appearance of sporadic dot fluorescence indicated that the A $\beta$  plaques in the brain parenchyma could be partially labeled. After that, the dot fluorescence became more apparent and the intensity reached the maximum at approximately 2 min, suggesting that the parenchymal A $\beta$  plaques could be nearly completely stained in 2 min. Notably, the plaques' fluorescence could be sustained for over 10 min, while the vessels' fluorescence decayed from the circulation and clearance of probe 9, which could produce distinct fluorescence to visualize the distribution of A $\beta$  plaques in the brain parenchyma. In addition to parenchymal A $\beta$  plaques, CAAs in the

large vessels could also be labeled and clearly pinpointed by probe 9 after 10 min. After 20 min, the bright plaques' fluorescence in the parenchyma decreased significantly, presumably owing to the clearance of probe 9 from the brain parenchyma, while CAAs' fluorescence remained visible throughout the vessels. In contrast, neither parenchymal A $\beta$  plaques' fluorescence nor CAAs' fluorescence appeared in the age-matched WT mouse during the time course of imaging due to the lack of A $\beta$  plaques both in brain parenchyma and blood vessels (Figure S50), according to the results from both *in vivo* fluorescence imaging of mice (Figure 6) and *in vitro* fluorescence staining of resected brain tissue slices (Figure S34 and Figure S35). These dynamic epifluorescence imaging results intuitively suggested that probe 9 could rapidly cross the BBB and efficiently label both the parenchymal and angiopathic A $\beta$  plaques in APP/PS1 AD mouse, not WT mouse, supporting the high potential of our designed probes for noninvasively detecting A $\beta$  deposits *in vivo*.

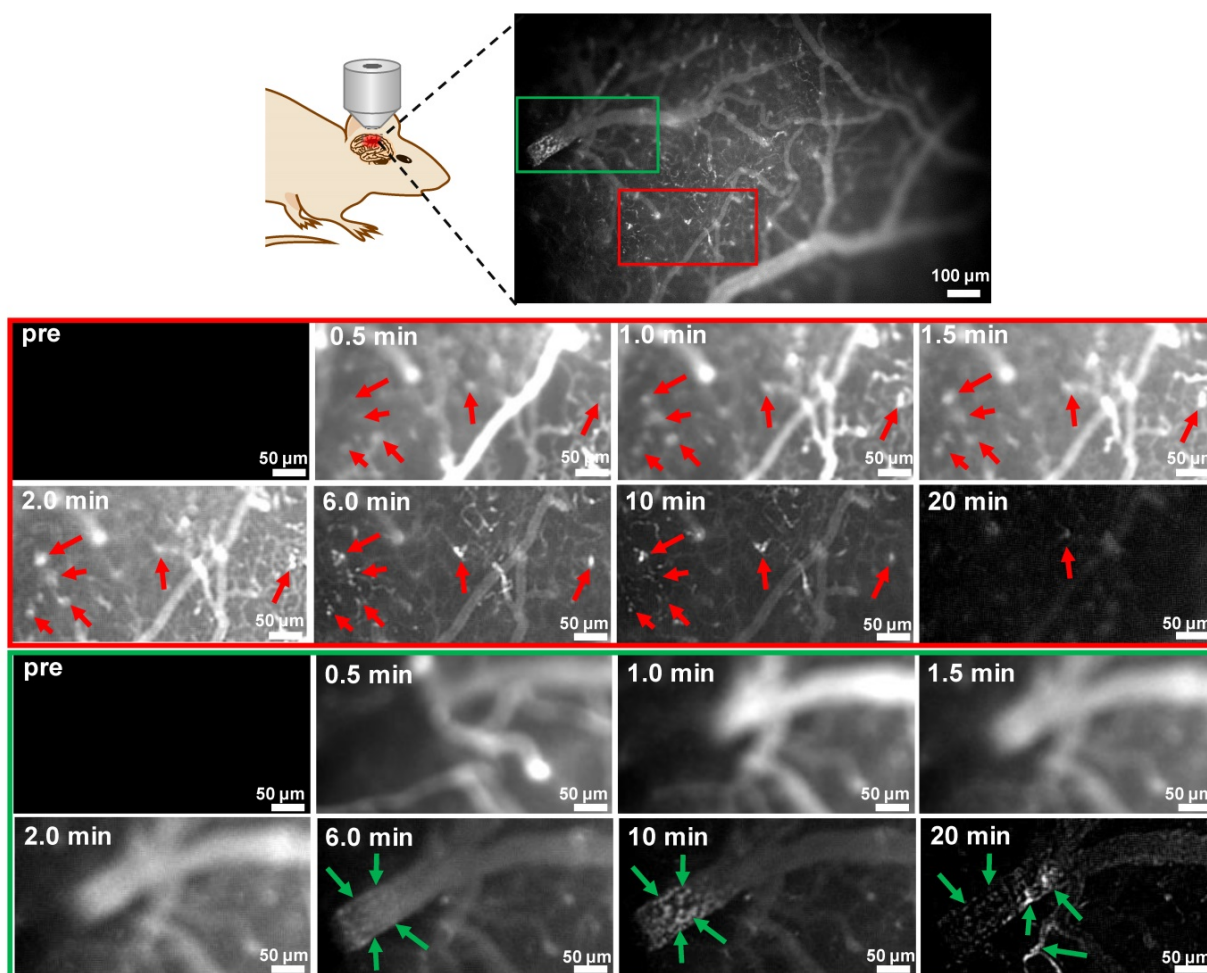


**Figure 7.** Dynamic FL imaging of A $\beta$  plaques in the brain of a skull-thinning 14-month-old APP/PS1 mouse following i.v. injection of probe 9 (1.0 mg/kg). The fluorescence images were monitored every 5 s on an upright fluorescent microscope. Red and green rectangles indicated enlarged brain parenchyma area and cerebral vessel, respectively. Red arrows indicated the A $\beta$  plaques in the brain parenchyma; green arrows indicated the CAAs in the cerebral vessel.

## The attenuation effect of probe 9 on the aggregation of A $\beta$ monomers

As mentioned above, probe 9 possessed good binding affinity to A $\beta$  monomers ( $K_d = 11.16 \pm 0.79$  nM) and oligomers ( $K_d = 36.59 \pm 2.69$  nM), it is crucial to assay whether the binding could slow or even prevent the propagation of soluble A $\beta$  species into A $\beta$  aggregates. The western blot analysis (Figure S51) demonstrated that probe 9 was able to attenuate the aggregation of A $\beta$  monomers in a concentration-dependent manner and probe 9 exhibited a significantly higher attenuation effect than CRANAD-58. There was no significant amount of high molecular weight species observed on the SDS-PAGE gel, presumably due to that A $\beta$ 42 could aggregate fast into insoluble species that are too large to enter the gel [18].

## Discussion

As a good NIR fluorescent probe for A $\beta$  species, the following properties should be satisfied: (1) high specificity and affinity to A $\beta$  species, (2) reasonable lipophilicity ( $\log P$  between 1 and 3) to guarantee rapid Blood-Brain-Barrier (BBB) penetrability, (3) the “turn-on” fluorescence emission wavelength >650 nm to minimize background fluorescence from brain tissue, (5) high quantum yield, (6) low nonspecific binding, (7) reasonable stability, (8) straightforward synthesis, and most importantly, (9) upon binding to A $\beta$  species, a significant change in fluorescent properties should be observed. To date, a variety of fluorescent probes able to target A $\beta$  species have been reported, such as AOI-987 [57], NIAD-4 [35], CRANAD-2 [17], BAP-1 [36], THK-265 [58], PAD-1 [59], CQ [30], BD-Oligo [60], F-SLOH [61], QAD-1 [33], QM-FN-SO<sub>3</sub> [62], TM-1 [31], DANIRs [22-27, 32, 37], CAQ [63], PTO-29 [21], PTO-41 [47], CRANAD-3 [19], CRANAD-102 [20] and CRANAD-58 [18]. Nevertheless, none of them meet all of these criteria due to some potential shortcomings, such as limited BBB permeability of charged molecules, shallow penetration depth or autofluorescence resulting from relative short fluorescence wavelength, slow binding kinetics and relative high  $K_d$  values. In addition, some of these reported probes are only responsive to insoluble A $\beta$  aggregates and plaques on the late stage of AD (Table S2), which is not conducive to the early diagnosis and treatment of the neurodegenerative disease. Among these probes, CRANAD-58 was reported to have the capability to detect both soluble and insoluble A $\beta$  species, which is vital to monitor the changes of A $\beta$  species during the pathological course of the disease. Though CRANAD-58 has shown promise to noninvasively detect A $\beta$  species in transgenic AD mice, the emission wavelength (~670

nm) is still too short for further applications. Therefore, new probes with longer emission wavelength and improved physiological properties are in highly demand.

In the research, through rationally hybridizing CRANAD-58 and NIR cyanine IR-780 fluorophore, we have developed nine D-A-D type of NIR fluorescent probes (1-9) for noninvasive imaging of both soluble and insoluble A $\beta$  species in living APP/PS1 AD mice. Based on the modification step-by-step, probe 9 was demonstrated to be optimum probe due to its fast kinetically binding with A $\beta$  species (< 120 s), high sensitivity and selectivity towards A $\beta$  species. Owing to a more efficient delocalization of electrons from 1,3,3-trimethyl-indoline group, probe 9 showed longer emission wavelength (A $\beta$  monomers: 690 nm v.s. 674 nm, oligomers: 688 nm v.s. 667 nm, aggregates: 697 nm v.s. 675 nm) upon interaction with A $\beta$  species, compared with that of CRANAD-58. In addition, probe 9 showed significant fluorescence intensity enhancement upon binding to A $\beta$  species acted as 1:1 molar ratio, which indicated a “turn-on” fluorescent response towards A $\beta$  species. Moreover, probe 9 possesses desirable lipophilicity ( $\log P = 2.14$ ), which significantly enhanced the brain uptake. It should be noticed that probe 9 (~20.31) also have a higher quantum yield than CRANAD-58 (~9.58) in CH<sub>2</sub>Cl<sub>2</sub>, which is a typical solvent to mimic the hydrophobic microenvironment of the A $\beta$  species. The western blot analysis indicated that probe 9 possessed significantly higher attenuation effect than CRANAD-58 in concentration-dependent manner, suggestive of its potential for the treatment of AD. Based on these findings, probe 9 hold the following outstanding features: (1) To be an excellent NIR fluorescence probe, probe 9 meets the properties required for monitoring soluble and insoluble A $\beta$  species noninvasively *in vivo*, and thus possessed great potential to early definitive diagnosis of AD and monitoring anti-AD drugs' efficacy *in vivo*; (2) Probe 9 showed red-shifted emission wavelength than CRANAD-58, which was conducive to enhance penetration depth and improve sensitivity for *in vivo* imaging, especially for the noninvasive fluorescence imaging of brain, where the intact cranium existed; (3) Probe 9 also showed higher quantum yield than CRANAD-58, which indicated that a lower administration dose for probe 9 than that of CRANAD-58 was viable in the *in vivo* application and thus could reduce the neurotoxicity resulting from the relative high injection dose; (4) Probe 9 also showed significantly higher attenuation effect on the aggregation of A $\beta$  monomers than CRANAD-58 in concentration-dependent manner, indicated that

probe **9** might be used as imaging/therapeutic agent.

## Conclusion

In conclusion, we have developed nine D-A-D type of NIR fluorescent probes (**1-9**) for noninvasive imaging of both soluble and insoluble A $\beta$  species in living APP/PS1 AD mice. We first designed probes **1** and **2** by rationally hybridizing CRANAD-58 and NIR cyanine IR-780 fluorophore, and demonstrated that probe **2** deemed to be optimum over probe **1** and CRANAD-58 because it showed a higher fluorescence quantum yield ( $\Phi_f = \sim 26.3\%$ ) and longer fluorescence emission ( $\lambda_{ex/em} = 619/675$  nm) than probe **1** ( $\Phi_f = \sim 13.2\%$ ,  $\lambda_{ex/em} = 614/659$  nm) or CRANAD-58 ( $\Phi_f = \sim 9.6\%$ ,  $\lambda_{ex/em} = 581/653$  nm) in CH<sub>2</sub>Cl<sub>2</sub>. Probe **2** also showed larger fluorescence turn-on ratios upon binding with one equivalent of A $\beta$  monomers, oligomers and aggregates, respectively, with the fluorescence emissions all extending to over 690 nm, longer than that of CRANAD-58 ( $\sim 670$  nm). Titration and <sup>1</sup>H-NMR spectroscopic studies demonstrated that probe **2** could probably bind to the KLVFF fragment in the A $\beta$  species, allowing fast binding kinetics, good binding affinity, high sensitivity and specificity to detect both soluble and insoluble A $\beta$  species. After i.v. injection, it can rapidly penetrate the BBB and produce approximately 1.3-fold higher brain fluorescence in APP/PS1 AD mice than that in the age-matched WT mice at 10 min, which increased to  $\sim 1.5$ -fold at 30 min. The *ex vivo* fluorescence imaging of brain tissue slices resected from APP/PS1 mouse at 30 min post i.v. injection showed that probe **2** could label A $\beta$  species deposited in hippocampus, cerebral cortex, cerebellum area and cerebral vessels. In order to augment the bathochromic effect and improve the *in vivo* imaging performance, further structural modification of probe **2** to afford probes **3-9** was then conducted. These seven probes displayed different fluorescence response and binding affinities toward A $\beta$  monomers, oligomers and aggregates. Among them, probe **4** displayed larger fluorescence turn-on ratio than probe **2** upon incubation with A $\beta$  species *in vitro*, which could produce significantly  $\sim 2.0$ -fold higher fluorescence intensity in the brain of APP/PS1 mice compared to that in the WT mice at 10 min. Probe **6** with a 3-methoxy group as the H-bond acceptor exhibited higher binding affinities toward A $\beta$  monomer ( $K_d = 3.01 \pm 0.41$  nM), A $\beta$  oligomer ( $K_d = 25.62 \pm 1.54$  nM) and A $\beta$  aggregates ( $K_d = 13.51 \pm 0.73$  nM) compared to other probes. However, *in vivo* imaging results showed a longer time ( $\sim 60$  min) to peak brain fluorescence and slower washout from brain. It was notable that probe **9** with a slightly reduced log*P* value hold the fastest kinetics ( $\sim 10$  min) to maximize brain fluorescence in the APP/PS1 mice,

with intensity higher than that of probes **2**, **4**, **6** and CRANAD-58. Particularly, probe **9** hold great potential to discriminate 6-month-old (predominant soluble A $\beta$  species) or 10-month-old (predominant insoluble A $\beta$  species) APP/PS1 AD mice from age-matched WT mice, with signal intensity ratio of APP/PS1 AD mice to WT mice being  $\sim 1.5$  and  $\sim 1.7$  at 10 min respectively. Furthermore, dynamic fluorescence imaging of the skull-thinning APP/PS1 AD mouse on an upright fluorescent microscope demonstrated that probe **9** could immediately cross the BBB and selectively map the A $\beta$  plaques in both brain parenchyma and cerebral angiopathic areas. Overall, our results demonstrated that our designed “off-on” NIR fluorescence probes could be efficient to detect both soluble and insoluble A $\beta$  species *in vivo*, potential for applications in early diagnosis of AD and noninvasive evaluation of anti-AD drugs’ efficacy *in vivo*.

## Abbreviations

AD: Alzheimer’s disease; A $\beta$ : amyloid- $\beta$ ; ThT: thioflavin T; MRI: magnetic resonance imaging; SPECT: single-photon emission-computed tomography; PET: positron emission computed tomography; NIR: near infrared; BODIPY: boron dipyrromethane; BBB: blood brain barrier; HOMO: highest occupied molecular orbital; LUMO: lowest unoccupied molecular orbital; APP/PS1: APP<sup>swe</sup>/PSEN1; WT: wild type; DMEM: dulbecco’s modified eagle’s medium; FBS: fetal bovine serum; MTT: methyl thiazolyl tetrazolium; HFIP: hexafluoroisopropanol; TEM: transmission electron microscopy; PTA: phosphotungstic acid; LOD: limit of detection; AChE: acetylcholinesterase; BuChE: Butyrylcholinesterase; GSH: glutathione; BSA: Bovine serum albumin; CAAs: cerebral amyloid angiopathies.

## Supplementary Material

Supplementary methods, figures, tables, NMR and MS spectra. <https://www.thno.org/v12p3178s1.pdf>

Supplementary Movie 1 - APP-PS1 mouse.

<https://www.thno.org/v12p3178s2.mp4>

Supplementary Movie 2 - WT mouse.

<https://www.thno.org/v12p3178s3.mp4>

## Acknowledgements

Financial supports from the National Natural Science Foundation of China (21632008 and 21922406), Natural Science Foundation of Jiangsu Province (BK20190055) and Excellent Research Program of Nanjing University (ZYJH004) are acknowledged.

## Author Contributions

Daqing Fang and Xidan Wen performed the experiments, interpreted the data. Yuqi Wang, Yidan Sun and Ruibing An participated part of the experiments and analyzed the data. Deju Ye and Daqing Fang wrote the manuscript. Hong Liu, Deju Ye and Yu Zhou designed the study, interpreted the data and supervised the project. All of the authors have read and approved the final manuscript.

## Competing Interests

The authors have declared that no competing interest exists.

## References

- Blennow K, de Leon MJ, Zetterberg H. Alzheimer's disease. *The Lancet*. 2006; 368: 387-403.
- Querfurth HW, LaFerla FM. Alzheimer's disease. *N Engl J Med*. 2010; 362: 329-44.
- Selkoe DJ. Alzheimer's Disease: Genes, Proteins, and Therapy. *Physiol Rev*. 2001; 81: 741-66.
- Klein WL, Krafft GA, Finch CE. Targeting small A $\beta$  oligomers: the solution to an Alzheimer's disease conundrum? *Trends Neurosci*. 2001; 24: 219-24.
- McLean CA, Cherny RA, Fraser FW, Fuller SJ, Smith MJ, Konrad V, et al. Soluble pool of A $\beta$  amyloid as a determinant of severity of neurodegeneration in Alzheimer's disease. *Ann Neurol*. 1999; 46: 860-6.
- Haass C, Selkoe DJ. Soluble protein oligomers in neurodegeneration: lessons from the Alzheimer's amyloid beta-peptide. *Nat Rev Mol Cell Biol*. 2007; 8: 101-12.
- Higuchi M, Iwata N, Matsuba Y, Sato K, Sasamoto K, Saido TC. <sup>19</sup>F and <sup>1</sup>H MRI detection of amyloid beta plaques *in vivo*. *Nat Neurosci*. 2005; 8: 527-33.
- Ono M, Saji H. SPECT imaging agents for detecting cerebral  $\beta$ -amyloid plaques. *Int J Mol Imaging*. 2011; 2011: 543267.
- Rowe CC, Villemagne VL. Brain amyloid imaging. *J Nucl Med*. 2011; 52: 1733-40.
- Staderini M, Martin MA, Bolognesi ML, Menendez JC. Imaging of  $\beta$ -amyloid plaques by near infrared fluorescent tracers: a new frontier for chemical neuroscience. *Chem Soc Rev*. 2015; 44: 1807-19.
- Klunk WE, Engler H, Nordberg A, Wang Y, Blomqvist G, Holt DP, et al. Imaging brain amyloid in Alzheimer's disease with Pittsburgh Compound-B. *Ann Neurol*. 2004; 55: 306-19.
- Choi SR, Golding G, Zhuang Z, Zhang W, Lim N, Hefti F, et al. Preclinical properties of <sup>18</sup>F-AV-45: a PET agent for A $\beta$  plaques in the brain. *J Nucl Med*. 2009; 50: 1887-94.
- Clark CM, Schneider JA, Bedell BJ, Beach TG, Bilker WB, Mintun MA, et al. Use of florbetapir-PET for imaging  $\beta$ -amyloid pathology. *JAMA*. 2011; 305: 275-83.
- Landau SM, Thomas BA, Thurfjell L, Schmidt M, Margolin R, Mintun M, et al. Amyloid PET imaging in Alzheimer's disease: a comparison of three radiotracers. *Eur J Nucl Med Mol*. 2014; 41: 1398-407.
- Tong H, Lou K, Wang W. Near-infrared fluorescent probes for imaging of amyloid plaques in Alzheimer's disease. *Acta Pharm Sin B*. 2015; 5: 25-33.
- Raymond SB, Skoch J, Hills ID, Nesterov EE, Swager TM, Bacskai BJ. Smart optical probes for near-infrared fluorescence imaging of Alzheimer's disease pathology. *Eur J Nucl Med Mol Imaging*. 2008; 35: 93-8.
- Ran C, Xu X, Raymond SB, Ferrara BJ, Neal K, Bacskai BJ, et al. Design, synthesis, and testing of difluoroboron-derivatized curcumins as near-infrared probes for *in vivo* detection of amyloid- $\beta$  deposits. *J Am Chem Soc*. 2009; 131: 15257-61.
- Zhang X, Tian Y, Li Z, Tian X, Sun H, Liu H, et al. Design and synthesis of curcumin analogues for *in vivo* fluorescence imaging and inhibiting copper-induced cross-linking of amyloid beta species in Alzheimer's disease. *J Am Chem Soc*. 2013; 135: 16397-409.
- Zhang X, Tian Y, Zhang C, Tian X, Ross AW, Moir RD, et al. Near-infrared fluorescence molecular imaging of amyloid beta species and monitoring therapy in animal models of Alzheimer's disease. *Proc Natl Acad Sci U. S. A*. 2015; 112: 9734-9.
- Li Y, Yang J, Liu H, Yang J, Du L, Feng H, et al. Tuning the stereo-hindrance of a curcumin scaffold for the selective imaging of the soluble forms of amyloid beta species. *Chem Sci*. 2017; 8: 7710-7.
- Yang J, Zeng F, Li X, Ran C, Xu Y, Li Y. Highly specific detection of A $\beta$  oligomers in early Alzheimer's disease by a near-infrared fluorescent probe with a "V-shaped" spatial conformation. *Chem Commun*. 2020; 56: 583-6.
- Fu H, Cui M, Tu P, Pan Z, Liu B. Evaluation of molecules based on the electron donor-acceptor architecture as near-infrared  $\beta$ -amyloid-targeting probes. *Chem Commun*. 2014; 50: 11875-8.
- Zhou K, Fu H, Feng L, Cui M, Dai J, Liu B. The synthesis and evaluation of near-infrared probes with barbituric acid acceptors for *in vivo* detection of amyloid plaques. *Chem Commun*. 2015; 51: 11665-8.
- Fu HL, Cui MC, Zhao L, Tu PY, Zhou KX, Dai JP, et al. Highly sensitive near-infrared fluorophores for *in vivo* detection of amyloid- $\beta$  plaques in Alzheimer's disease. *J Med Chem*. 2015; 58: 6972-83.
- Fu H, Tu P, Zhao L, Dai J, Liu B, Cui M. Amyloid- $\beta$  deposits target efficient near-infrared fluorescent probes: synthesis, *in vitro* evaluation, and *in vivo* imaging. *Anal Chem*. 2016; 88: 1944-50.
- Zhou KX, Bai HC, Feng L, Dai JP, Cui MC. Smart D- $\pi$ -A type near-infrared A $\beta$  probes: effects of a marked  $\pi$  bridge on optical and biological properties. *Anal Chem*. 2017; 89: 9432-7.
- Zhou K, Li Y, Peng Y, Cui X, Dai J, Cui M. Structure-property relationships of polyethylene glycol modified fluorophore as near-infrared A $\beta$  imaging probes. *Anal Chem*. 2018; 90: 8576-82.
- Yan JW, Zhu JY, Zhou KX, Wang JS, Tan HY, Xu ZY, et al. Neutral merocyanine dyes: for *in vivo* NIR fluorescence imaging of amyloid- $\beta$  plaques. *Chem Commun*. 2017; 53: 9910-3.
- Rajasekhar K, Narayanaswamy N, Murugan NA, Kuang G, Ågren H, Govindaraju T. A high affinity red fluorescence and colorimetric probe for amyloid  $\beta$  aggregates. *Sci Rep*. 2016; 6: 23668.
- Rajasekhar K, Narayanaswamy N, Murugan NA, Viccaro K, Lee HG, Shah K, et al. A $\beta$  plaque-selective NIR fluorescence probe to differentiate Alzheimer's disease from tauopathies. *Biosens Bioelectron*. 2017; 98: 54-61.
- Xu M, Li R, Li X, Lv G, Li S, Sun A, et al. NIR fluorescent probes with good water-solubility for detection of amyloid beta aggregates in Alzheimer's disease. *J Mater Chem B*. 2019; 7: 5535-40.
- Zhou KX, Yuan C, Dai B, Wang K, Chen YM, Ma DL, et al. Environment-sensitive near-infrared probe for fluorescent discrimination of A $\beta$  and Tau fibrils in AD brain. *J Med Chem*. 2019; 62: 6694-704.
- Ren WM, Zhang JJ, Peng C, Xiang HJ, Chen JJ, Peng CY, et al. Fluorescent imaging of  $\beta$ -amyloid using BODIPY based near-infrared off-on fluorescent probe. *Bioconjugate Chem*. 2018; 29: 3459-66.
- Watanabe H, Ono M, Matsumura K, Yoshimura M, Kimura H, Saji H. Molecular imaging of  $\beta$ -amyloid plaques with near-infrared boron dipyrromethane (BODIPY)-based fluorescent probes. *Mol Imaging*. 2013; 12: 338-47.
- Nesterov EE, Skoch J, Hyman BT, Klunk WE, Bacskai BJ, Swager TM. *In vivo* optical imaging of amyloid aggregates in brain: design of fluorescent markers. *Angew Chem Int Ed*. 2005; 44: 5452-6.
- Ono M, Watanabe H, Kimura H, Saji H. BODIPY-based molecular probe for imaging of cerebral  $\beta$ -amyloid plaques. *ACS Chem Neurosci*. 2012; 3: 319-24.
- Cui MC, Ono M, Watanabe H, Kimura H, Liu BL, Saji H. Smart near-infrared fluorescence probes with donor-acceptor structure for *in vivo* detection of  $\beta$ -amyloid deposits. *J Am Chem Soc*. 2014; 136: 3388-94.
- Zhang X, Tian Y, Yuan P, Li Y, Yaseen MA, Grutzendler J, et al. A bifunctional curcumin analogue for two-photon imaging and inhibiting crosslinking of amyloid beta in Alzheimer's disease. *Chem Commun*. 2014; 50: 11550-3.
- Kayed R, Head E, Thompson JL, McIntire TM, Milton SC, Cotman CW, et al. Common structure of soluble amyloid oligomers implies common mechanism of pathogenesis. *Science*. 2003; 300: 486-9.
- Marker DF, Tremblay M, Lu S, Majewska AK, Gelbard HA. A Thin-skull window technique for chronic two-photon *in vivo* imaging of murine microglia in models of neuroinflammation. *JoVE*. 2010; 43: e2059.
- Wan Q, Chen S, Shi W, Li L, Ma H. Lysosomal pH rise during heat shock monitored by a lysosome-targeting near-infrared ratiometric fluorescent probe. *Angew Chem Int Ed*. 2014; 53: 10916-20.
- Choi HS, Nasr K, Alyabyev S, Feith D, Lee JH, Kim SH, et al. Synthesis and *in vivo* fate of zwitterionic near-infrared fluorophores. *Angew Chem Int Ed*. 2011; 50: 6258-63.
- Zhao XX, Li LL, Zhao Y, An HW, Cai Q, Lang JY, et al. *In situ* self-assembled nanofibers precisely target cancer-associated fibroblasts for improved tumor imaging. *Angew Chem Int Ed*. 2019; 58: 15287-94.
- Wang Y, Hu X, Weng J, Li J, Fan Q, Zhang Y, et al. A photoacoustic probe for the imaging of tumor apoptosis by caspase-mediated macrocyclization and self-assembly. *Angew Chem Int Ed*. 2019; 58: 4886-90.
- Polishchuk V, Stanko M, Kulinich A, Shandura M. D- $\pi$ -A- $\pi$ -D dyes with a 1,3,2-dioxaborine cycle in the polymethine chain: efficient long-wavelength fluorophores. *Eur J Org Chem*. 2018; 2018: 240-6.
- Cosco ED, Spearman AL, Ramakrishnan S, Lingg JGP, Saccomano M, Pengshung M, et al. Shortwave infrared polymethine fluorophores matched to excitation lasers enable non-invasive, multicolour *in vivo* imaging in real time. *Nat Chem*. 2020; 12: 1123-30.
- Zeng F, Yang J, Li X, Peng K, Ran C, Xu Y, et al. Versatile near-infrared fluorescent probe for *in vivo* detection of A $\beta$  oligomers. *Bioorg Med Chem*. 2020; 28: 115559.
- Petric A, Johnson SA, Pham HV, Li Y, Ceh S, Golobic A, et al. Dicyanovinyl naphthalenes for neuroimaging of amyloids and relationships of electronic structures and geometries to binding affinities. *Proc Natl Acad Sci U. S. A*. 2012; 109: 16492-7.
- Zhu JY, Zhou LF, Li YK, Chen SB, Yan JW, Zhang L. *In vivo* near-infrared fluorescence imaging of amyloid- $\beta$  plaques with a dicyanoisophorone-based probe. *Anal Chim Acta*. 2017; 961: 112-8.

50. Tan H, Zhou K, Yan J, Sun H, Pistolozzi M, Cui M, *et al.* Dual-functional red-emitting fluorescent probes for imaging beta-amyloid plaques and viscosity. *Sens Actuators, B.* 2019; 298: 126903.
51. Tan HY, Qiu YT, Sun H, Yan JW, Zhang L. A lysosome-targeting dual-functional fluorescent probe for imaging intracellular viscosity and beta-amyloid. *Chem Commun.* 2019; 55: 2688-91.
52. Yang HY, Zhang JJ, Zang Y, Zhang HY, Li J, Chen GR, *et al.* D-A-D fluorogenic probe for the rapid imaging of amyloid  $\beta$  plaques *in vivo*. *Dyes Pigm.* 2017; 136: 224-8.
53. Yang J, Zhu BY, Yin W, Han ZH, Zheng C, Wang P, *et al.* Differentiating A $\beta$ 40 and A $\beta$ 42 in amyloid plaques with a small molecule fluorescence probe. *Chem Sci.* 2020; 11: 5238-45.
54. Kumar-Singh S, Pirici D, McGowan E, Serneels S, Ceuterick C, Hardy J, *et al.* Dense-core plaques in Tg2576 and PSAPP mouse models of Alzheimer's disease are centered on vessel walls. *Am J Pathol.* 2005; 167: 527-43.
55. Sun H, Liu J, Li SL, Zhou LY, Wang JW, Liu LB, *et al.* Reactive amphiphilic conjugated polymers for inhibiting amyloid  $\beta$  assembly. *Angew Chem Int Ed.* 2019; 58: 5988-93.
56. Du Z, Yu DQ, Du XB, Scott P, Ren JS, Qu XG. Self-triggered click reaction in an Alzheimer's disease model: *in situ* bifunctional drug synthesis catalyzed by neurotoxic copper accumulated in amyloid- $\beta$  plaques. *Chem Sci.* 2019; 10: 10343-50.
57. Hintersteiner M, Enz A, Frey P, Jaton AL, Kinzy W, Kneuer R, *et al.* *In vivo* detection of amyloid- $\beta$  deposits by near-infrared imaging using an oxazine-derivative probe. *Nat Biotechnol.* 2005; 23: 577-83.
58. Okamura N, Mori M, Furumoto S, Yoshikawa T, Harada R, Ito S, *et al.* *In vivo* detection of amyloid plaques in the mouse brain using the near-infrared fluorescence probe THK-265. *J Alzheimer's Dis.* 2011; 23: 37-48.
59. Cheng Y, Zhu B, Deng Y, Zhang Z. *In vivo* detection of cerebral amyloid fibrils with smart dicyanomethylene-4h-pyran-based fluorescence probe. *Anal Chem.* 2015; 87: 4781-7.
60. Teoh CL, Su D, Sahu S, Yun SW, Drummond E, Prelli F, *et al.* Chemical fluorescent probe for detection of A $\beta$  oligomers. *J Am Chem Soc.* 2015; 137: 13503-9.
61. Li YH, Xu D, Sun AY, Ho SL, Poon CY, Chan HN, *et al.* Fluoro-substituted cyanine for reliable *in vivo* labelling of amyloid- $\beta$  oligomers and neuroprotection against amyloid- $\beta$  induced toxicity. *Chem Sci.* 2017; 8: 8279-84.
62. Fu W, Yan CX, Guo ZQ, Zhang JJ, Zhang HY, Tian H, *et al.* Rational design of near-infrared aggregation-induced-emission active probes: *in situ* mapping of amyloid- $\beta$  plaques with ultrasensitivity and high-fidelity. *J Am Chem Soc.* 2019; 141: 3171-7.
63. Wu J, Shao CW, Ye XL, Di XJ, Li DD, Zhao H, *et al.* *In vivo* brain imaging of amyloid- $\beta$  aggregates in Alzheimer's disease with a near-infrared fluorescent probe. *ACS Sens.* 2021; 6: 863-70.